Alma Mater Studiorum · Università di Bologna

Scuola di Scienze
Dipartimento di Fisica e Astronomia
Corso di Laurea in Astrofisica e Cosmologia

Effects of Type Ia Supernova feedback in young globular clusters

Relatore:
Chiar.mo Prof. Carlo Nipoti

Presentata da:
Marco Donati

Correlatori:
Dott. Francesco Calura
Dott.ssa Elena Lacchin

Sessione IV
Anno Accademico 2022/23

Contents

Chapter 1

Introduction

In the last few decades, extensive research using photometric and spectroscopic studies has revealed strong evidence of multiple stellar populations in all Galactic globular clusters (GGCs). From the theoretical point of view, the mechanisms which originated their multiple stellar populations are far from being clear. This Thesis aims to further the analysis of multiple stellar populations, building upon the work initiated by Calura et al. (2019). In that study, a simulation depicting the genesis of a second generation of stars in a massive globular cluster at high redshift, enriched chemically through self-enrichment in the asymptotic giant branch (AGB) scenario, was presented and analyzed. Later, Lacchin et al. (2021), starting from the setup of Calura et al. (2019), explored the role of Type Ia Supernovae on the formation of SG stars. They found that SNe Ia could significantly reduce the star formation and prevent the accretion of pristine gas onto the cluster altering the chemistry of both gas and newborn stars. Yaghoobi et al. (2022) complemented the work of Calura et al. (2019) by extending the analysis to lower-mass clusters and they conducted an observational comparison with GGCs finding good agreement between the observational dataset and the high-density simulations. This Thesis aims at studying the effects of SNe Ia on the star formation, as the one of Lacchin et al. (2020), on clusters with the same mass of Yaghoobi et al. (2022).

The structure of this Thesis is outlined as follows:

- Chapter 2 provides a background on the physical context of the thesis. It summarizes the main properties of globular clusters, with a focus on the phenomenon of multiple stellar populations. Additionally, it briefly describes Type Ia supernovae, as this Thesis is focused on the role played by these particular type of supernova explosion on the formation of globular clusters.

- Chapter 3 reviews the essential features of RAMSES, the hydrodynamic code employed for the simulations whose results will be presented in the thesis. Furthermore, it outlines the physical components implemented in the

customized version, including AGB feedback, cooling, star formation, and SNeIa feedback. Finally it briefly defines the simulation setup.

- Chapter 4 encompasses the analysis of simulation data. Spatial maps of the gaseous and stellar components, as well as density profiles, are presented at different time points. Special attention is given to the temporal variations in chemical abundances.

- Chapter 5 provides the conclusions of this Thesis.

Chapter 2

Multiple Populations in Globular Clusters

This chapter digs into the intricacies of globular clusters, astronomical objects that have long piqued the interest of astronomers due to their elusive nature. Stars, rather than choosing isolation, frequently aggregate in clusters, which could be subdivided in open and globular clusters. Open clusters are characterized by young and loosely bound stars, while globular clusters (GCs) are populated by millions of densely packed stars in nearly spherical formations (Lada & Lada 2003). Despite exhaustive studies, these clusters remain enigmatic, for example concerning their motion and dynamics. Initially perceived as symmetric, isotropic, and non-rotating, recent technological advancements, such as high-resolution photometry and multi-object spectroscopy, have revealed complexities like varying speeds and internal rotation, challenging the notion that these clusters are immutable. In the last decades, another notable revelation questioned the previous assumption of uniformity, suggesting that most, if not all, GCs have experienced multiple episodes of star formation, which are the main focus of this thesis.

In this chapter, we will point out the fundamental characteristics of GCs with a primary focus on revealing the processes governing their formation and their initial evolutionary phases.

2.1 Globular clusters: main properties

Globular clusters are dynamically bound structures with a stellar potential composed of approximately 10^{5-6} stars, mainly concentrated in the center of this nearly spherical system with a diameter ranging from 20 to 100 pc. Our galaxy, the Milky Way (MW), hosts more than 150 of these clusters, primarily distributed between the halo and bulge. These objects are dated among the oldest stellar components of the MW and tipically host stars older than 10 Gyr.

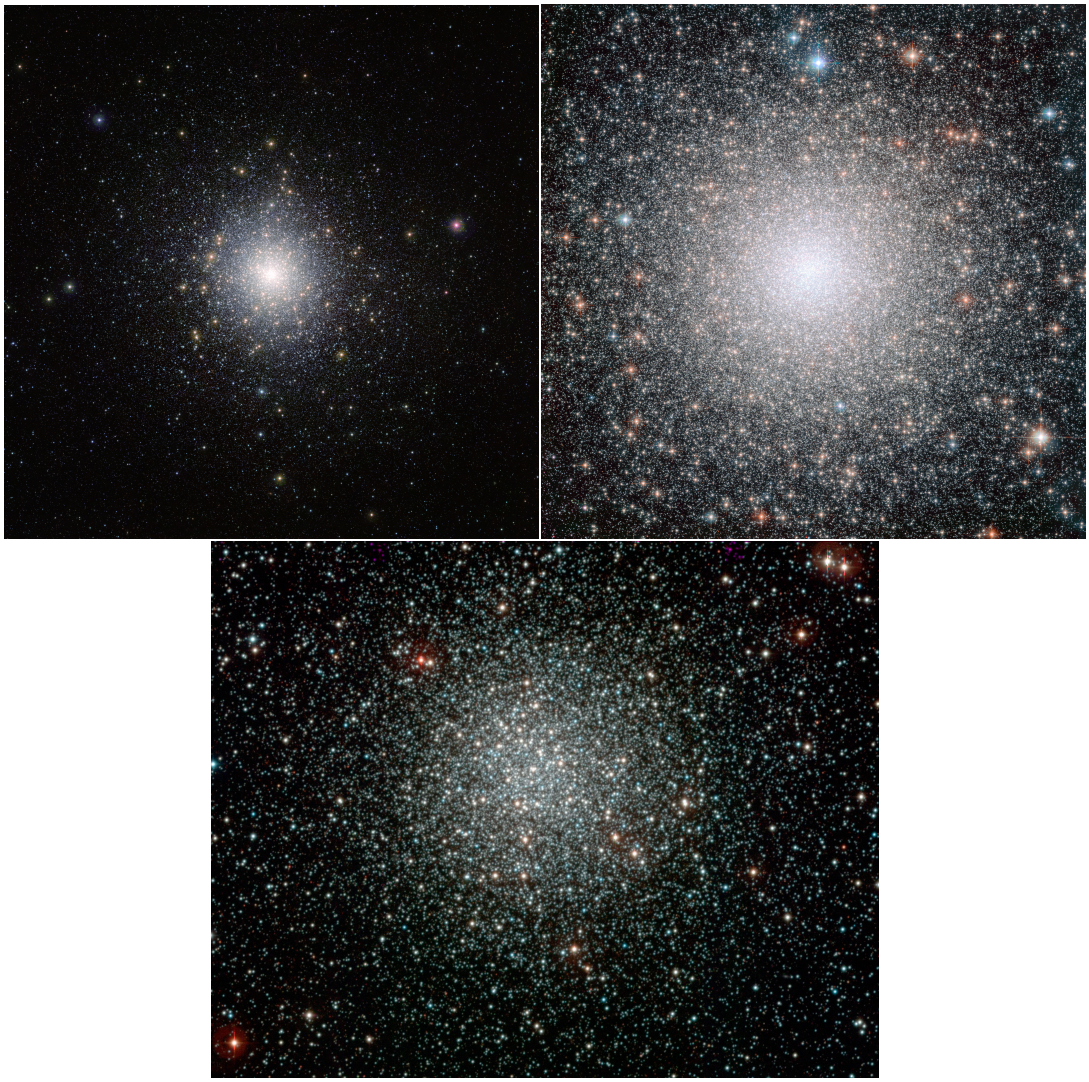

Figure 2.1. Three examples of galactic globular clusters (GGCs). *Top row*: (*left*) 47 Tucanae (VISTA), (*left*) NGC6388(Hubble). *Bottom row*: NGC3201 (MPG/ESO 2.2-metre telescope). Credits: ESO.

Until a few decades ago, observations led to the assumption that stars within these clusters were chemically homogeneous and coeval, making them suitable for modeling through the Simple Stellar Population (SSP) model, a single generation of stars formed simultaneously in a burst of star formation (Renzini & Buzzoni (1986)). However, with the continuous advancement of observational facilities and improved data analysis tools a different and more complex picture has emerged. Numerous spectroscopic studies have revealed that Galactic globular clusters host stellar populations that exhibit chemical inhomogeneity. This is consistent with the presence of multiple stellar populations (MPs), which are combinations of SSPs with different ages (Bastian & Lardo 2018). Figure 2.2 illustrates the example of the globular cluster NGC 2808 that was initially thought to be homogeneous and coeval. Observed again, about a decade ago, the cluster now reveals the presence of multiple stellar populations with distinct chemical abundances.

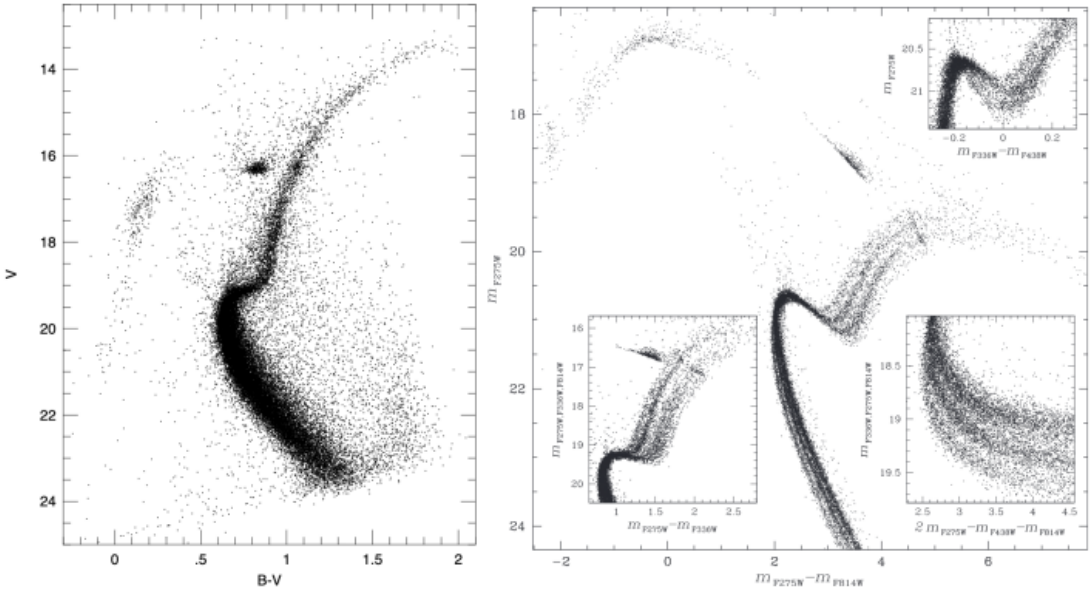

Figure 2.2. Color-magnitude diagrams (CMD) showcasing the globular cluster NGC 2808, captured by the ground-based 4m Blanco telescope (left panel, Walker 1999) and from observations using the Hubble Space Telescope (right panel, Milone et al. 2015).

Now, let's explore the characteristics that distinguish the various populations of stars in globular clusters.

2.2 Multiple stellar populations

It is currently well established that most, and possibly all, globular clusters (GCs) have a significant diversity in the chemical abundances of stars and among the

clusters. Within these clusters, the multiple populations (MPs) exhibit variations in their abundance of light elements. An "anomalous" component is typically characterized by enhancements in He, N, and Na abundances, coupled with depletions in C and O compared to the field stars of the host galaxy (Minniti et al. 1993, Carretta et al. 2009, Gratton, R. G. et al. 2013, Marino et al. 2014 and Gratton et al. 2019 and references therein), while generally the different populations share similar iron content (Gratton et al., 2004).

While observational progress has brought to light and confirmed the existence of these MPs, a comprehensive model explaining their formation is yet to be established. Several models have been proposed to account for their origins, but none has yet provided a complete explanation for all the observed trends and features in GCs.

In the next subsection, I will explore the formation of multiple populations of stars in GCs, discussing some of the most studied models in the literature, with a specific emphasis on the scenario employed in this thesis, the AGB scenario.

2.2.1 The formation of multiple populations

As previously defined, what sets apart the MPs are their distinct chemical abundances. Changes in chemistry with respect to the first population of stars can occur through two different enrichment scenarios, both of which involve the first population stars as polluters.

Self-enrichment In this scenario, first population stars release enriched material that is then recycled to form new stars. According to this hypothesis, distinct populations of stars are associated with different generations. The first population is therefore a first generation (FG) consists of coeval stars resembling a SSP, while the the chemically anomalous stars, called second generation (SG) is composed of stars exhibiting anomalous chemical compositions, such as enhanced Na and depleted O. In the literature, several scenarios assume a self-enrichment to explain the MP phenomenon, such as the Asymptotic Giant Branch (AGB) scenario (D'Ercole et al. 2008; Calura et al. 2019; Lacchin et al. 2021 and Yaghoobi et al. 2022), the Fast Rotating Massive Stars (FRMS) scenario (Decressin et al., 2007b), the Massive Interacting Binary (MIB) scenario (de Mink et al., 2009), and the Super Massive Star (SMS) scenario (Denissenkov & Hartwick, 2014).

Single star formation Different stellar populations are formed at the same time and are therefore coeval. Bastian et al. 2013b proposed that first population stars eject enriched material that is accreted onto protostellar cores of low mass stars. In this case, stars with different chemical abundances will be coeval with the

"polluters." Scenarios assuming a single star formation episode include the MIB scenario (Bastian et al., 2013a) and the SMS scenario (Gieles et al., 2018).
Other scenarios studied in the literature, which I will not describe in this chapter, involve polluters different from the FG stars. To cite a few examples, Elmegreen (2017) explores massive stars, Breen (2018) uses black hole accretion disks and Wang et al. (2020) considers stellar mergers.

Each scenario must be able to reproduce observational constraints, such as the observed anticorrelations in chemical abundances, as well as the number of stars formed in the new populations. A common issue in these models is the mass budget problem, as they all exhibit an insufficient gas emission from first population stars and, consequently,the second population mass would be much less than what is observed. For this reason, it is assumed that the mass of the precursor GC must have been initially larger than that of present-day clusters.

2.2.2 Asymptotic Giant Branch scenario

The most widely used model for the formation of multiple populations, known as the AGB scenario, was first introduced by Cottrell & Da Costa (1981). Over the years, this model has undergone modifications and improvements to better align with observational constraints. Subsequently, these enhancements have been introduced in other scenarios.

As this is the model employed in the analyzed simulation of this thesis, before defining the entire scenario in all its aspects, I provide a brief description of the AGB stellar phase, with particular emphasis on its role in enriching the surrounding gas.

2.2.2.1 AGB stars

The AGB stellar phase, initiated by the burning of helium in the stellar core, is characterized by double-shell burning, involving fusion reactions on the helium and hydrogen shells. This phase comprises two stages: 1) the early AGB phase, where the ignition of the helium layer causes the expansion of the envelope, interrupting the burning of hydrogen and helium. This stage also triggers convective motions, the second dredge-up (SDU), for masses greater than $4\,M_{\odot}$, enriching the envelope with a substantial amount of helium. 2) Thermal pulses, where the gas falls resulting from the previous expansion contracts the hydrogen shell and restarts the nuclear reactions. The helium created in this phase forms a degenerate helium shell, which, under suitable conditions, reactivates helium burning, establishing a cycle with timescales of 10^{3-5}yr depending on the mass. Additionally, the third dredge-up (TDU) occurs in this phase, bringing additional carbon and oxygen to the surface. If the stellar mass exceeds 3 solar masses, the appearance of O^{16} and

Mg^{25} is possible due to conditions favorable for slow neutron captures. Finally, for stars with masses greater than 4-5 $M_\odot$ and at the bottom of the convective envelope a temperature of $\sim 8 \cdot 10^7$ K, the hot bottom burning (HBB) takes place. This phenomenon involves the conversion of C^{12} into N^{14}, contributing to the anticorrelation mentioned in Section 2.2, and the formation of Li^7, which is then brought to the surface through convective motions.

The final abundance of the star is shaped by the dominant mechanisms,which depend on temperature, mass, and metallicity. The TDU process transports He-burning products like C, Ne and O to the stellar surface. In contrast, hot bottom burning primarily transports hydrogen-burning products, leading to a reduction in O levels and an increase in Na abundance.

2.2.2.2 The AGB scenario

In this scenario, a FG of coeval and chemically homogeneous stars formed in the disk of a star forming high-redshift galaxy, constituting a cluster orbiting within a galaxy. After approximately 40 Myr, it is assumed that all massive stars have exploded as core-collapse SNe, carving a whole in the disk of the host galaxy, leaving behind intermediate and low-mass stars in the asymptotic giant branch phase and the ISM begins to fall into the potential well of the FG stars. The timescale for this process is contingent upon the ISM density of the host galaxy. Simultaneously, material ejected by the newly formed AGB stars, at lower velocities than the escape velocity (v=10-30 km/s), is also falling toward the center of the potential well (cooling flow). This dense, cold, and enriched gas reservoir confined in the center is used to generate SG stars. Hence, in this model, the incorporation of pristine gas accreted by the cluster is crucial for explaining the observed proportions of FG to SG masses and their current abundance pattern. D'Ercole et al. (2011) demonstrated that the substantial reservoir of pristine gas is essential for diluting the AGB ejecta, thereby elucidating the correlations between light elements.

In Fig. 2.3, the formation of MPs in the globular cluster according to this scenario is schematically illustrated.

2.2.3 Fast Rotating Massive Stars scenario

The Fast Rotating Massive Stars (FRMS) model proposes a self-enrichment scenario involving stars with masses ranging from 20 $M_\odot$ to 120 $M_\odot$, which can generate high-temperature H-burning products along the main sequence (MS), and rotation speeds comparable to the break-up speed at the stellar surface (v=600-1000 km/s). Beyond this speed, centrifugal force overcomes the gravitational field of the star, resulting in the expulsion of stellar material. These ejected materials

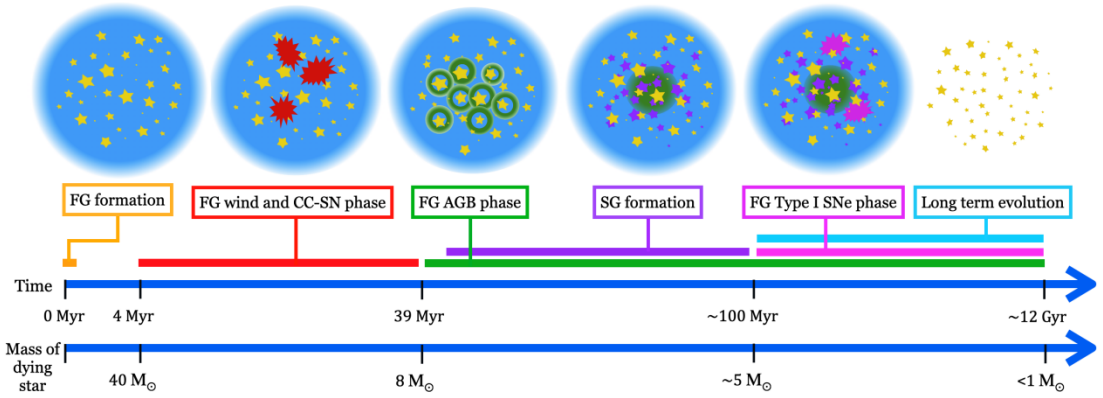

Figure 2.3. Schematic representation of the various stages in the formation of MPs in a Gc under the AGB scenario. The illustration emphasizes the primary feedback sources at different points in time and the associated mass of the dying star. Credits: *Elena Lacchin*.

are thought to mix with pristine gas, forming the second-generation stars in the immediate vicinity of the massive star polluters (Prantzos, N. & Charbonnel, C. 2006; Decressin et al. 2007a,b). In contrast to the AGB model, gas enrichment occurs rapidly, with a time difference of approximately 3.5 Myr between the formation of the first and second generations (Krause et al. 2013). The enrichment process concludes with the explosion of the first CC-SNe from the FG, leading to the ejection of most of the gas from the cluster and contamination with iron (Decressin et al. 2007b). Regarding the chemical composition of these SG stars in this scenario, it will depend on the time available for FRMS to undergo internal convective motions (SDU). Initially releasing pristine gas, it gradually expels more H-burning products drawn from the stellar interior layers over time.

In order to overcome the mass budget problem, Charbonnel et al. (2014) proposed a variation of the model introducing a modification to this scenario. They proposed that FG stars were initially formed with a top-heavy initial mass function (IMF), resulting in their death by the present time. Consequently, what is conventionally referred to as the FG is actually an SG formed from material not enriched by the H-burning products.

One possible observational hint of FRMS has been found in NGC 5253-5 where the nitrogen enrichment detected in the HII region surrounding the cluster has been explained by Roy et al. (2020) with the combined effects of a high mass and rotation of FG stars.

2.2.4 Massive Interacting Binary scenario

The massive binary scenario, as proposed by de Mink et al. (2009), suggests massive interacting binaries with stellar masses ranging from 10 to 100 $M_{\odot}$ as the sources

of enriched material. In this scenario, the primary star, being the more massive component of the binary system, undergoes evolution into a giant star, causing an expansion in its diameter that overcomes the Roche lobe. This expansion leads to the transfer of material to the secondary star. The mass loss, driven by the conservation of angular momentum, allows the secondary star to reach the break-up velocity (observationally v= 30-70 km/s), enriching the gas in the stellar cluster. Following this phase, the primary star undergoes a substantial loss of its envelope, leading to the ignition of helium in the core and its transformation into a Wolf-Rayet star. Simultaneously, the secondary star experiences a decrease in its rotational velocity. Furthermore, a second event of enrichment occurs as a result of the expansion of the primary star triggered by He-shell burning.

Regarding the chemical composition of these SG stars in this scenario, similar to the previous scenario, the ejecta abundances will depend on time. As the primary star evolves, so does the chemical composition of the ejected material, starting from H-burning products to material showing He enhancement and the Na-O anticorrelation.

2.2.5 Super Massive Star scenario

This scenario involves massive FG stars that would be present if the IMF is flatter.

Super Massive Stars are formed in the central region of the cluster during the very early stages of star formation. The mass of the cluster enables it to accumulate a significant amount of gas by increasing its central density and reducing the two-body relaxation time of the system. This leads to star collisions dominating and causing the system to expand. Once newly generated stars initiate stellar feedback, gas accretion and the initial phase of star formation will cease. SMS evolution will eventually bring stars into the zero-age main-sequence (ZAMS) phase, during which material accreted by collisions is processed, mixed by convection, and emitted by stellar wind. These stars are thought to explode by SN pair-instability or collapse into a black hole, as He-burning products are not observed in GCs.

Denissenkov & Hartwick (2014) discusses how stars formed by SMS-enriched gas retrieve good agreement with the light-element anticorrelations observed in GCs.

The presence of intermediate massive black holes is thought to be related to the existence of these stars (Lützgendorf et al., 2013). However, both these families remain theoretical for now.

2.3 Type Ia Supernovae

One main feature of the simulation analyzed in this thesis is the presence of Type Ia supernova (SN Ia) feedback, which influences the star formation of the cluster and affects its metallicity. Before delving into how it is implemented in this scenario, it is useful to briefly define the physical phenomenon.

A Type Ia supernova explosion occurs in the context of a binary system of low and intermediate-mass stars ($M<8\,M_{\odot}$), where at least one evolved star, a CO white dwarf, accretes mass through mass transfer or merging, and triggering the nuclear fusion of carbon in the degenerate core. The explosion happens when the pressure of degenerate material in the WD is no more able to contrast its gravitational pull. This could happen before the WD reaches the Chandrasekar mass, leading to a sub-Chandrasekar explosion, or at the Chandrasekar mass, leading to a near-Chandrasekar one. In both cases, the explosion can involve a WD and a non-degenerate star (single degenerate scenario) or two WDs (double degenerate scenario): 1) the single degenerate scenario in which the primary star, already evolved into a white dwarf, is accreting material from its younger companion. 2) In the double degenerate scenario, both stars become white dwarfs, and the emission of gravitational waves brings the two stars closer until they merge. In this Thesis we will consider only the near-Chandrasekar channel and the single degenerate scenario as they are the dominant contributors to the Type Ia SNe explosions in the timespan of our simulations.

Both scenarios involve carbon fusion for the supernova to initiate and the material emitted by this process consists almost entirely of Fe^{56} gas.

In subsection 3.4.3, we will explore the role of SNeIa in this context, outlining their implementation in the simulation code. The integration of this phenomenon into the AGB scenario of multiple population formation was initially introduced by D'Ercole et al. (2008), and in this work, we refer to the adjustments detailed in Lacchin et al. (2021).

2.4 Aim of this thesis

In summary, this thesis focuses on the study of star formation of multiple stellar populations in globular clusters orbiting a high-redshift star forming galaxy. To define the chemical anomalies of newborn stars, our observational constraint, we refer to a self-enrichment scenario, specifically the AGB scenario, taking into account the potential contribution of SNeIa.

In order to analyze this scenario, a series of simulations have been conducted implementing the mentioned features, the details of which are explored in the next chapter, and its thesis represents its anlysis. The aim of this work (as already

discussed in Calura et al. 2019; Lacchin et al. 2021 and Yaghoobi et al. 2022) is to gain a deeper understanding of the properties characterizing these systems examining the effects of Type Ia supernovae on clusters of different masses, both on the intensity of star formation and on the chemical composition of newborn stars. Such investigations are essential for interpreting the new wealth of data anticipated from present-day and future instruments, including JWST and the Extremely Large Telescope.

Chapter 3

Numerical simulations

Among the numerous scientific challenges faced in astrophysics, the analysis and comprehension of globular clusters formation and evolution constitute a pivotal chapter. Anyway, due to the intricate and diverse nature of the physical processes involved in GC formation, in models the use of an analyical approach is not feasible. For instance, while the Bondi-Hoyle-Lyttleton formula (Bondi 1952) allows for an estimate of the mass accretion rate for a point mass accretor, a comparable simple analytical formula for the accretion onto potentials with extended mass distributions is lacking and resorting to numerical simulations becomes necessary. Widely used now, such simulations help understand the highly non-linear nature of various processes (e. g. star formation, cooling, feedback), and in the literature, different algorithms with specific applications in various fields can be found.

These algorithms can be categorized into hydrodynamical solvers for computing fluid dynamics and Poisson solvers for computing gravitational interactions. To carry out the simulation analyzed in this thesis, we utilized the RAMSES code, a widely employed tool for astrophysical hydrodynamic simulations equipped with a N-body solver.

This Chapter starts with a quick overview of hydrodynamics and N-body numerical methods, then I delve into how these concepts are incorporated into the RAMSES code and I also detail the specific physical processes integrated into the simulated scenario. Finally, I will walk through the simulation setup, outlining the initial conditions of the modelled system.

3.1 Principles of hydrodynamical solvers

While present-day globular clusters are considered gas-poor systems, the analysis of their hydrodynamics becomes crucial during their formation and in the initial phases of their evolution. In this scenario, indeed, significant streams of matter and rapid variations in hydrodynamic variables occur due to the stellar potential, along with the injection of energy and turbulent activity from supernovae.

In order to apply fluid dynamics to the system's gas, it is essential to assume that the gas is composed of fluid elements meeting the following criteria:

- The fluid element is sufficiently small (ℓ_{region}) than the characterstic scale ℓ_{scale} over which any macroscopic quantity q varies

$$\ell_{\text{region}} \ll \ell_{\text{scale}} \sim \frac{q}{|\nabla q|}$$

- It is large enough to contain many particles, allowing us to ignore fluctuations due to a finite number of particles n

$$n\ell_{\text{region}}^3 \gg 1$$

- More importantly, the system is collisional, meaning the mean free path λ is much smaller than any scale of interest

$$\ell_{\text{region}} \gg \lambda$$

In most cases astrophysical gas is collisional and effectively well described as a fluid. Moreover, at the typical temperatures, densities, and pressures commonly encountered in the evolution of galaxies and clusters, the gas can be treated as an ideal gas .

The dynamics of the gas in our system are described through the three conservation laws in the Eulerian form for a non-viscous and compressible gas:

$$\frac{\partial \rho}{\partial t} + \nabla \cdot (\rho \vec{u}) = 0 \tag{3.1}$$

$$\frac{\partial}{\partial t}(\rho \vec{u}) + \nabla \cdot (\rho \vec{u} \otimes \vec{u}) + \nabla p = -\rho \nabla \phi \tag{3.2}$$

$$\frac{\partial}{\partial t}(\rho e) + \nabla \cdot [\rho \vec{u}(e + p/\rho)] = -\rho \vec{u} \cdot \nabla \phi + \frac{\Gamma - \Lambda}{\rho} \tag{3.3}$$

where ρ is the mass density, $\vec{u}$ is the velocity, p is the thermal pressure, e is the specific total energy, ϕ is the gravitational potential, Γ and Λ are the heating and

cooling rates, respectively. Furthermore, the energy term (e) can be split into a kinetic and internal energy (ϵ) components and p can be expressed in terms of it:

$$e = \frac{\vec{u}^2}{2} + \varepsilon \tag{3.4}$$

$$p = (\gamma - 1)\rho(e - \frac{1}{2}u^2) = (\gamma - 1)\rho\varepsilon \tag{3.5}$$

where γ is the adiabatic index, which is equal to $5/3$ for a monoatomic gas. It's worth noting that the energy equation (3.3) is conservative for the total fluid energy, if one ignores the source terms due to gravity and gas cooling/heating. This property is one of the main advantages of solving the Euler equations in conservative form: no energy sink due to numerical errors can alter the flow dynamics.

The numerical solution of these equations is approached through the discretization of time, which is inevitable, as well as space. The analyzed fluid is divided using a grid so that each cell represents an element of fluid in which it is possible to evaluate each hydrodynamic variable and their derivatives at fixed point. In the early algorithms, such as ZEUS (Stone & Norman 1992), the grid was constructed uniformly for simplicity but suffered from low-resolution issues, especially if needed only locally (e.g., shocks, SN bubbles). This problem significantly strains the temporal integration of the simulation. To address this difficulty, since the late '80s, non-uniform adaptive grid techniques such as Adaptive Mesh Refinement (AMR) have been used, where higher resolutions are applied only in cells that satisfy certain conditions. While this approach is beneficial in terms of computational costs, crucial in the numerical domain, the simplicity of the code is compromised due to the necessity of handling cells with varying sizes. The code used for the simulation discussed in this thesis, RAMSES (Teyssier 2002), also incorporates AMR; in the next section, we'll take a closer look at how it operates. Other well-known codes in the literature that adopt a similar AMR-type grid include ENZO (Bryan et al. 2014), FLASH (Fryxell et al. 2000), ART (Kravtsov et al. 1997), ATHENA (Stone et al. 2008), along with its updated version ATHENA++ (Stone et al. 2020), NIRVANA (Ziegler 2005), and PLUTO (Mignone et al. 2007).

Although not necessary for describing the algorithm used to conduct the simulation under analysis, it is worthwhile to provide a brief overview of the Lagrangian formalism and its interpretation in a numerical context. In contrast to the Eulerian framework, in the Lagrangian approach, the fluid is split into parcels, or particles that move through space and time. Mathematically, this shift in perspective is captured by the advective derivative

$$\frac{\mathrm{D}}{\mathrm{D}t} \equiv \frac{\partial}{\partial t} + u \cdot \nabla$$

and a reformulation of the Eulerian equations takes the following form:

$$\frac{D\rho}{Dt} + \rho\nabla \cdot \vec{u} = 0 \tag{3.6}$$

$$\frac{D}{Dt}(\rho\vec{u}) = -\nabla p - \rho\nabla\phi \tag{3.7}$$

$$\frac{D}{Dt}(\rho e) + \rho e\nabla \cdot \vec{u} + \rho(e + p/\rho)\nabla \cdot \vec{u} = -\rho\vec{u} \cdot \nabla\phi + \frac{\Gamma - \Lambda}{\rho} \tag{3.8}$$

In this approach the fluid variables and their derivatives are computed in the reference frame that comoves with them and the predominant computational approach for such simulations involves smoothed-particle hydrodynamics. In this method, a discrete set of particles represents the continuous fluid, allowing the determination of gas properties at any point within the computational box by averaging their quantities over a specified number of neighboring particles. To cite a few example of Lagrangian codes, GADGET (Springel et al. 2001), GIZMO (Hopkins et al. 2010), GEAR (Revaz & Jablonka 2012), CHANGA (Menon et al. 2015), PHANTOM (Price et al. 2018).

3.2 Principles of N-Body solvers

The stars in a globular cluster are gravitationally bound, especially concentrated in the central regions. Therefore, they constitute the dominant component of the gravitational potential in this self-gravitating system. Consequently, to study the formation of star clusters, it becomes crucial to establish an accurate and efficient method for calculating the system's potential over time. For this purpose, in general one employs N-body method that evaluates the gravitational dynamics of the system, taking into account each mass element (*particle*) within the system. The numerical translation of Newton's gravitational theory, a prerequisite for obtaining simulated systems with a scientific value, justifies the multitude of methods and algorithms found in the literature.

Firstly, to mention one of the challenges faced by these methods, the nature of the gravitational force implies that if the distance between two particles tends to zero, the force - and hence the potential - diverges, requiring much smaller timesteps for the interaction compared to the rest of the system. This problem is addressed by adopting the softening method, which mitigates forces at short distances by replacing point masses with mass distributions, resulting in the cancellation of force for distances approaching zero (Fig. 3.1). For this purpose, the softening kernel function K_{soft} (Dehnen 2001) is introduced to modify the Newtonian potential:

$$\phi_{soft} = GmK_{soft}(\vec{x} - \vec{x}')$$

Where a frequently used form in the literature for K_{soft} is the Plummer Softening (Aarseth 1963):

$$K_{soft} = -\frac{1}{\sqrt{|\vec{x} - \vec{x}'|^2 + \epsilon^2}}$$

where ϕ represent the potential, G the gravitational constant, m mass of the particle, x position of the particle, ϵ softening length. In this way, the gravitational potential of each particle is that of a Plummer sphere with a scale length ϵ, defined as the softening length. The criteria for determining the value of ϵ are diverse and specific to the analyzed physical case (e.g., Dehnen 2001).

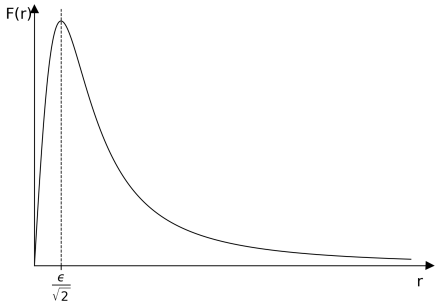

Figure 3.1. *Radial force in Plummer softening.*

Now, having the formula for the gravitational potential between two particles, let's explore some iterative methods to calculate the overall potential of the system.

The simplest of these methods, known as direct summation or particle-particle (PP), calculates the force field by summing, for each particle, all the forces obtained, according to Newton's law, from each pair of particles. Once the dynamics of each element is defined, the kinematics is updated accordingly. This approach, based on the formulas of gravitational theory, makes it undoubtedly the most accurate method but comes with a significant integration time. The PP method, indeed, requires a number of operations per timestep proportional to the square of the system's number of bodies ($\mathcal{O}(N^2)$). While it is suitable for the analysis of small-scale systems with a limited number of objects, typically up to 10^6, it is not suitable for greater gravitational systems like massive star clusters or more chaotic phenomena such as galaxy mergers.

A less accurate but faster method commonly used in literature is the particle-mesh (PM) technique, where the particle system is transformed into a grid (or "mesh") of density, and the Poisson equation is solved in the Fourier space using a Fast Fourier Transform algorithm. While not effective for simulating short-range interactions, the PM method is enhanced by the particle-particle-mesh (P^3M) approach, which employs the particle-particle method under a threshold radius value. Subsequently, another improvement to the method, known as Adaptive P^3M (AP^3M), was developed in Couchman (1991). This enhancement incorporates AMR, providing better resolution and accuracy in analyzing denser regions, such as in a clustering scenario, at the expense of a drastic increase in CPU time.

Another method, first introduced by Barnes & Hut (1986), is the Treecode. In this method, after organizing the particles into cells, the field is calculated by directly summing the contributions between nearby particles and approximating

those from more distant particles. The particle organization involves a hierarchical tree structure of cubic cells, where each cell can have up to eight subnodes corresponding to octants. This method has the advantage of not relying on a grid, making it efficient in simulating phenomena like galaxy mergers, where dense stellar systems move within nearly empty volumes.

3.3 RAMSES

As mentioned in previous chapters, this thesis work involves analyzing data from a simulation conducted using the RAMSES code. After establishing the fundamental concepts of numerical methods, this section introduces the main features of RAMSES (Teyssier 2002). The modules used in RAMSES can be categorized into four parts: the Adaptive Mesh Refinement (AMR) routines, the Particle Mesh routines, the Poisson solver routines, and the hydrodynamical routines. The following paragraphs will provide a brief explanation of each of these four parts and, at last, the time integration method.

3.3.1 Adaptive Mesh Refinement

The key data structure is a Fully Threaded Tree (FTT), introduced by Khokhlov (1998), which, instead of individual cells, the basic elements are groups of 2^{dim} (dim=3 in our scenario) sibling cells called octs, associated with a refinement level labeled as l. The base of the tree structure is a regular Cartesian grid, referred to as the *coarse grid* corresponding to $l = 0$. To efficiently access octs at a specific level, they are organized into a double-linked list. Each oct at level l points to its previous and next oct in the level linked list, but also to the parent cells at level l - 1, the two neighboring parent cells at level l - 1, and the 2^{dim} child octs at level $l + 1$. A graphical representation of this structure is shown in Figure 3.2.

The process begins with marking cells for refinement based on user-defined criteria, following a strict rule that dictates any oct in the tree structure must be surrounded by 3^{dim}-1 neighboring parent cells. This process involves three passages through each level, starting from the finest level l_{max} and descending to the coarse grid at $l = 0$:

- If a split cell contains a children cell that is marked or already refined, then mark it for refinement.
- Mark the 3^{dim}-1 neighboring cells.
- Mark any cell that meets the user-defined refinement criteria.

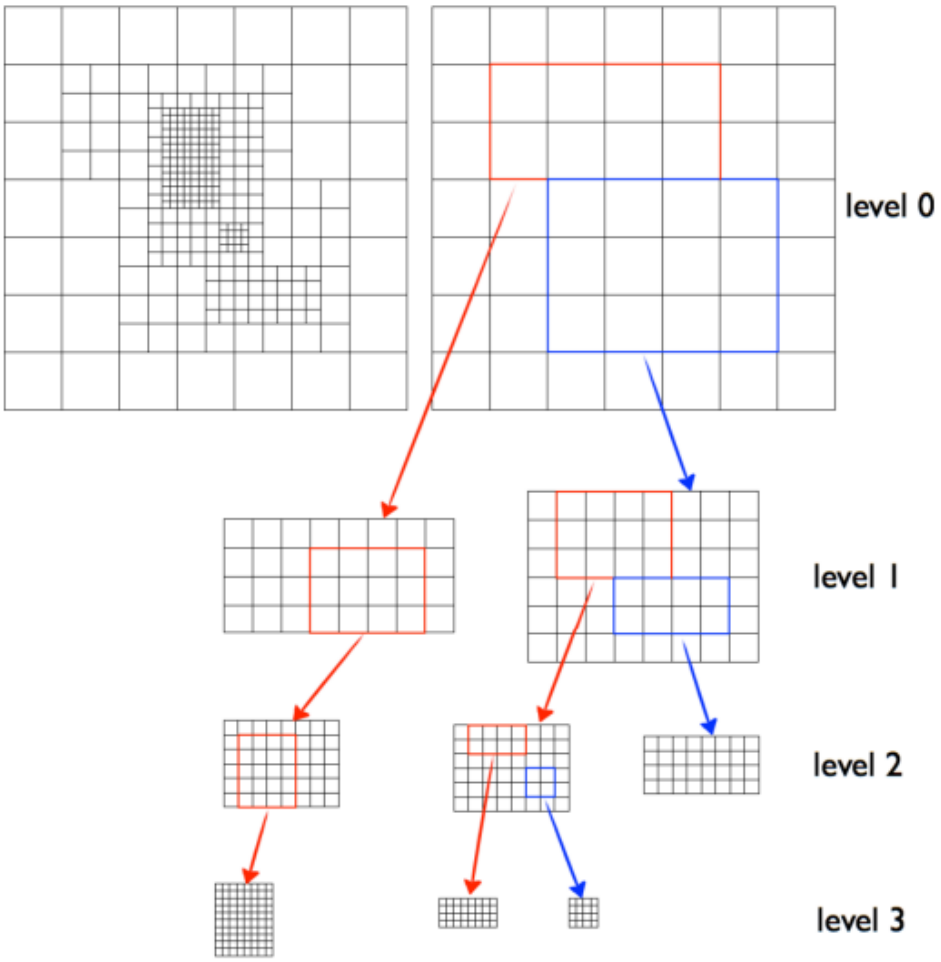

Figure 3.2. Schematic representation of the Fully Threaded Tree (FTT) process on a 2D Cartesian grid. Credits: *Fernando Becerra*.

Finally, the last step consists in splitting or destroying children cells according to the refinement map, identifying the leaf cells (cells without child octs) marked for refinement, creating its child octs, and identifying the split cells not marked for refinement and destroying the corresponding child octs.

3.3.2 Particle Mesh

Among the aforementioned N-body methods, Ramses exploits the PM one, which is based on the following steps:

1. Estimating mass density on the mesh using a "Cloud-In-Cell" (CIC) interpolation scheme.

2. Solving the Poisson equation to determine the potential across the mesh.
3. Calculating mesh acceleration via a standard finite-difference gradient approximation.
4. Determining individual particle acceleration using an inverse CIC interpolation method.
5. Adjusting particle velocity based on computed acceleration.
6. Updating particle positions in accordance with their velocities.

The Cloud-in-Cell (CIC) method, introduced by Hockney & Eastwood 1981, projects particle mass onto a mesh in two steps. Unlike a straightforward approach, CIC treats particles as finite-sized clouds, allowing their mass to overlap and spread across nearby cells, regardless of refinement levels. The algorithm considers particles at all levels and assigns mass to a cell based on the volume occupied by the associated cloud. This approach improves the representation of particle mass, considering spatial distributions and facilitating a smoother transition between discrete grid points within the mesh.

3.3.3 Poisson solver

In RAMSES, a 'one-way interface' scheme (Jessop et al. 1994; Kravtsov et al. 1997 with the ART code) is employed for solving the Poisson equation where the coarse grid solution never "sees" the effect of the fine grids. The coarsest level, a uniform Cartesian grid covering the computational box, utilizes the Fast Fourier Transform (FFT) technique (Hockney & Eastwood 1981) to efficiently solve the Poisson equation. The 'one-way interface' allows the coarse grid solution to influence finer grids' boundary conditions and initial guesses. RAMSES uses specific boundary conditions, solving the Poisson equation on the coarse grid with FFT which is faster than relaxation methods, required on finer grids, and then employing the Gauss-Seidel method with Red-Black Ordering and Successive Over Relaxation (Press et al. 1992) for potential computation.

Once the potential is obtained, the acceleration is computed using a 5-point finite difference algorithm to derive the cell-centered gradient of the potential. Subsequently, to assign each particle its acceleration, an inverse Cloud-in-Cell (CIC) scheme is applied.

3.3.4 Hydrodynamics

RAMSES employs an Eulerian hydrodynamic formalism (Eqs. 3.1; 3.2; 3.3), and its discretization takes the following form:

$$\frac{U_i^{n+1} - U_i^n}{\Delta t} + \frac{\mathcal{F}_{i+1/2}^{n+1/2} - \mathcal{F}_{i-1/2}^{n+1/2}}{\Delta x} = S_i^{n+1/2}$$

where U_i^n denote a numerical approximation to the cell averaged value of $(\rho, \rho\vec{u}, \rho e)$ at time t^n and for cell i, $\mathcal{F}_{i+1/2}^{n+1/2}$ are the time centered fluxes at the cell-edges and $S_i^{n+1/2}$ are the gravitational source-terms. The time-centered fluxes are computed using a second-order Godunov method, specifically the Piecewise Linear Method (Toro 1997) while gravitational source terms are implemented using a time-centered, fractional step approach:

$$S_i^{n+1/2} = \left(0, \frac{\rho_i^n \nabla\phi_i^n + \rho_i^{n+1}\nabla\phi_i^{n+1}}{2}, \frac{(\rho u)_i^n \nabla\phi_i^n + (\rho u)_i^{n+1}\nabla\phi_i^{n+1}}{2}\right)$$

based on the work of Colella 1990 and Saltzman 1994.

3.3.5 Time integration

In a code combining N-body and hydrodynamical simulations, the ability to adapt to variable time steps is crucial. Although the conventional leapfrog scheme (Hockney & Eastwood 1981) is accurate, it lacks the flexibility to handle changing time steps. RAMSES tackles this challenge by incorporating a second-order midpoint scheme, seamlessly reverting to the second-order leapfrog scheme when time steps remain constant.

The stability of the time step is assured by accounting for constraints from N-body and hydrodynamic solvers, as represented by the following conditions:

$$\begin{aligned}
\Delta t_1^\ell &= C_1 \times \min_\ell(\Delta t_{\rm ff}) \\
\Delta t_2^\ell &= C_2 \times \Delta x^\ell / \max_\ell(v_p) \\
\Delta t_3^\ell &= C_3 \times \frac{a_{\rm exp}}{\dot{a}_{\rm exp}}
\end{aligned}$$

Here, C_1 and C_2 are both less than 1, representing the time step related to the minimum free-fall time (Δt_{ff}) and the dynamics (v_p) of particles in the AMR grid, respectively. The third condition accounts for cosmological early stages, during the linear regime of gravitational clustering, through an expansion factor (a_{exp}), with $C_3 \approx 10\%$. Finally, the Courant-Friedrichs-Lewy stability condition is expressed by:

$$\Delta t_4^\ell = {\rm cfl} \times \Delta x^\ell / \max_\ell(|u_x| + c, |u_y| + c, |u_z| + c)$$

where cfl < 1 is the Courant factor.

Moreover, the effective time step is determined by $\min(\Delta t_1^\ell, \Delta t_2^\ell, \Delta t_3^\ell, \Delta t_4^\ell)$.

3.4 Subgrid physical processes and simulation setup

Achieving the necessary resolution to simulate all the physical phenomena in an astrophysical system is almost always impossible. An algorithm with extremely high resolution, while gaining in physical accuracy, suffers from non-convergent numerical integration times. On the other hand, omitting the simulation of certain physical processes capable of modifying the analyzed physical system risks devaluing the simulation. Striking a balance between these two scenarios is the major challenge in computational physics.

To address this, numerical methods incorporate subgrid models, patches of code that implement the effects of physical processes at a smaller scale than the maximum resolution. Some examples of these processes are star formation, supernova feedback, stellar evolution, chemistry, cosmic rays, turbulence, black hole accretion, magnetic fields, cooling and heating processes, etc.

In the physical context of the simulation analyzed in this Thesis, focused on the formation of multiple populations within a globular cluster, the implemented physical processes include AGB feedback, star formation and the feedback from SNeIa, a unique feature central in this work. Another subgrid model implemented is the equilibrium cooling, using native implementation in the RAMSES code and CLOUDY which will not be described in this Thesis, for details refer to Calura et al. 2019.

In this section, I provide an overview of the key features associated with each of these ingredients. For a more comprehensive description of these processes, refer to Calura et al. (2019) and Lacchin et al. (2021).

3.4.1 AGB feedback

As described in Chapter 2, the formation scenario of the simulated clusters is the AGB scenario, where the primary component of the current stellar chemistry is derived from the material ejected by intermediate-mass first-generation stars. Here, I summarize how the AGB feedback has been implemented in RAMSES. For further details, refer to D'Ercole et al. (2008) and Calura et al. (2019).

The mass return of material ejected by AGB stars is modeled by introducing a source term into the mass conservation equation (Eq. 3.1). This contribution is expressed analytically by:

$$\dot{\rho}_{\star,\mathrm{AGB}} = \alpha \rho_*$$

where ρ_{star} is the stellar density of the FG, and α represents the specific mass return rate. FG stars are distributed following a Plummer (1911) mass density

profile:

$$\rho_*(r) = \frac{3M_{FG}}{4\pi\, a^3}\left(1+\frac{r^2}{a^2}\right)^{-\frac{5}{2}}$$

with M_{FG} mass of the FG stars and a Plummer scale radius. The quantity α is computed following the formalism of Ciotti et al. 1991, adopting a Kroupa IMF (Kroupa 2001) and analytically defined by:

$$\alpha(t_{yr}) = 0.065 \cdot t_{yr}^{-1.01}$$

as a function of the age t_{yr} (expressed in years)of the FG population, valid for times spanning from 30 Myr to 100 Myr (corresponding to the timescales of our simulations).

Regarding the yield and chemical composition of the ejected material, the code computes helium and iron abundances. Helium abundances are determined following Ventura & D'Antona (2011), adopting a metallicity of $Z_{FG}=10^{-3}$ for the FG and the pristine gas.

The energy injection from FG AGB stars is incorporated through the following source term:

$$S = 0.5\ \alpha\ \rho_*\ (3\sigma^2 + v^2 + v_{wind}^2)$$

Here, v denotes the fluid velocity, σ represents the velocity dispersion calculated for a Plummer sphere using Dejonghe (1987), and $v_{\rm wind} \approx 2\times10^6$ cm/s is the wind velocity for AGB stars according to D'Ercole et al. (2008). The source term S corresponds to the gas heating due to the feedback from FG AGB stars and is applied at each timestep to the fluid energy.

3.4.2 Star Formation

The choice of a star formation model significantly influences the study of Multiple MPs. In this case, the native implementation of RAMSES, extensively detailed in Rasera & Teyssier (2006), has been adopted.

According to this algorithm, cells meeting the conditions for star formation, being cold ($T < 2{\cdot}10^4$ K) and exhibiting a converging net flow ($\nabla{\cdot}\vec{u} < 0$), transform 90%, of the gas within the cell into a star particle. This process is modelled according to the Schmidt (1959) law:

$$\dot{\rho}_{*,SG} = \frac{\rho}{t_*}$$

where ρ represents the gas density in the cell, and $t_\star$ denotes the star formation timescale, directly linked to the free-fall time and computed as follows:

$$t_* = t_0\left(\frac{\rho}{\rho_0}\right)^{-1/2}$$

with t_0 and ρ_0 free parameters.

As demonstrated in D'Ercole et al. (2008), at these times, star formation, and so our results, is not strongly dependent on the $t_\star$ term. Therefore, in this simulation (consistent with Calura et al. 2019, Lacchin et al. 2021, Yaghoobi et al. 2022), it is uniformly set at the value of 100 Myr ($t_\star \approx 100$ Myr).

Each collisionless star particle forms with a mass $M_{\star,SG} = N \cdot m_0$, where N is a positive integer and m_0 is the minimum mass set at 0.1 $M_\odot$. The value of N is extracted from a Poisson distribution given by the formula:

$$P(N) = \frac{\lambda^N e^{-\lambda}}{N!}$$

with λ mean value:

$$\lambda = \left(\frac{\rho \Delta x^3}{m_0}\right) \frac{\Delta t}{t_\star}$$

where, in this context, Δt represents the timestep, whereas Δx is the cell size.

Furthermore, the newborn stars form at the center of the parent cell (see section 3.1) with chemistry and velocity matching those of the gas contained in the cell.

Finally, the associated mass, momentum, energy, and density attributed to the newborn star are conservatively subtracted from those of the parent cell, as well as from the passive tracers specifically designed to track the chemical composition of the gas.

3.4.3 SNeIa feedback

A pioneering work that implemented the feedback of SNeIa in an AGB framework is presented in D'Ercole et al. (2008). Through the creation and analysis of two 1D hydrodynamic simulations, comparing scenarios with and without the contribution of SNeIa, the study aimed to investigate the impact of SNeIa on the star formation dynamics within GCs.

The algorithm for implementing SNeIa used in this simulation follows the approach outlined in Lacchin et al. (2021). I will now summarize its main characteristics and outline its application to the physical systems studied in this thesis.

As mentioned in section 2.3, SNeIa originate from the thermonuclear explosion of white dwarfs in binary systems. In this simulation, we consider explosions that inject one Chandrasekhar mass (1.44 $M_\odot$) of gas, including 0.5 $M_\odot$ of iron (Scalzo et al. 2014), and a metallicity equal to 1. Additionally, the explosions release 10^{51} erg of thermal energy into the ISM.

The temporal distribution of these explosions is regulated by the delay time distribution (DTD) proposed by Greggio (2005), as expressed in their Equation 16,

for the single degenerate scenario. The DTD starts at 40 Myr after the formation of the FG stars. The rate of SNe Ia explosions is contingent on the mass of the system M_{FG} and the adopted IMF. For a Kroupa (2001) IMF, within the time span of interest (approximately 0.1 Gyr), it is estimated that a cluster with a mass of $M_{FG} = 10^5\,M_\odot$ would experience around 10 SN Ia events, while $M_{FG} = 10^6\,M_\odot$ would witness approximately 100 such explosions (Greggio 2005).

Regarding their spatial distribution, SNe Ia are expected to follow the one of the FG stars, and therefore a Plummer profile with M_{FG}=$10^{5-6}\,M_\odot$ and a= 3 pc. However, due to the limited number of these events, 1000 random realizations were generated for both their spatial and temporal distributions. The realization that exhibited the least deviation from the mean was then selected. This procedure is the same as the one used in Lacchin et al. 2021.

In Figure 3.3 and 3.4 we show the mean spatial and temporal distribution among these 1000 realizations in red at 1 and 2 σ and the chosen realization in blue for the low mass model ($M_{FG} = 10^5\,M_\odot$) and the high mass models ($M_{FG} = 10^6\,M_\odot$), respectively.

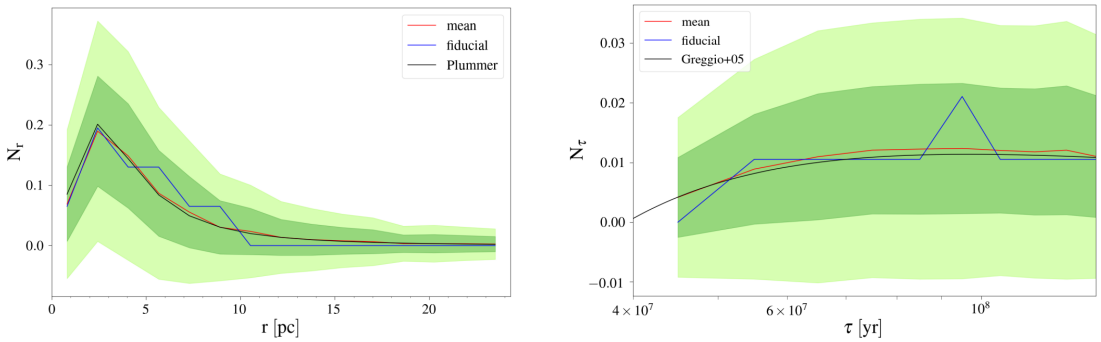

Figure 3.3. *Left panel*: Spatial distribution of Type Ia SNe as a function of the radius for a FG mass of $10^5\,M_\odot$. In black, we show the analytical result for the Plummer profile assuming $M_{\rm FG} = 10^5 M_\odot$ and a Plummer radius $a = 3$ pc. The red line indicates the mean of 1000 realizations with the associated regions within 1 and 2 σ in green and light green, respectively. The chosen realization is shown in blue, corresponding to the one that deviates less from the mean among the 1000 realizations. All the plotted lines are normalized, imposing $\int_0^{r_{\rm max}} N_r dr = 1$ with the maximum radius $r_{\rm max} = 25$ pc, which corresponds to half the size of the computational box. *Right panel*: Delay time distribution function. In black, we show the theoretical one from Eq.16 of Greggio (2005) assuming $\alpha = 2.35$ and $\gamma = 2$. The red line indicates the mean of 1000 realizations with the associated regions within 1 and 2 σ in green and light green, respectively. The chosen configuration among the 1000 realizations is shown in blue, namely the one that deviates less from the mean. The plotted lines are all normalized, imposing $\int_{\tau_i}^{\tau_x} N_\tau d\tau = 1$, where $\tau_i = 40$ Myr is the lifetime of an 8 $M_\odot$ star and $\tau_x = 140$ Myr, in order to cover the entire timespan we are focusing on, with the normalization factor in units of Gyr^{-1}. Credits: *Elena Lacchin.*

For further details regarding the computational physics behind the implemen-

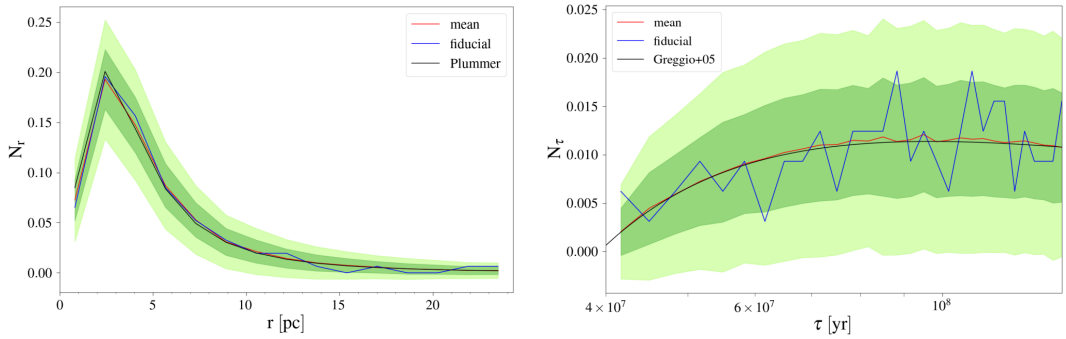

Figure 3.4. *Left panel*: Spatial distribution of Type Ia SNe as a function of the radius for a FG mass of $10^6\,M_\odot$. In black, we show the analytical result for the Plummer profile assuming $M_{\rm FG} = 10^6 M_\odot$ and a Plummer radius $a = 3$ pc. The red line indicates the mean of 1000 realizations with the associated regions within 1 and 2 σ in green and light green, respectively. The chosen realization is shown in blue. *Right panel*: Delay time distribution function. In black, we show the theoretical one from Eq.16 of Greggio 2005 assuming $\alpha = 2.35$ and $\gamma = 2$. The red line indicates the mean of 1000 realizations with the associated regions within 1 and 2 σ in green and light green, respectively. The chosen configuration among the 1000 realizations is shown in blue. Credits: *Elena Lacchin*.

tation of this subgrid model of SNeIa feedback, refer to the paper by Lacchin et al. (2021) and Lacchin's Ph.D. thesis (2023).

3.4.4 Simulation setup

The simulation setup coincides with Yaghoobi et al. (2022)'s one, with the addition of SNeIa feedback, following a similar approach as in Lacchin et al. (2021) and Calura et al. (2019).

The theoretical framework follows D'Ercole et al. (2016), which investigates the formation of a high-redshift globular cluster orbiting within a dwarf galaxy disk. As illustrated in Figure 3.5, the rapid formation of FG stars, occurring through collapse into an accretion disk, triggers successive SN II explosions from the first massive stars, generating a hot gas bubble termed a "superbubble." Over the initial tens of Myr, the continual injection of energy causes the bubble to expand, sweeping away the cluster's gas, dismantling the accretion disk, and dispersing enriched material from the bubble into the circum-galactic medium. In a disk galaxy after the blow-out of the bubble, the enriched material is preferentially ejected vertically due to the lack of resistance of the sorrounding ISM, not perturbed by the bubble. In the context of the AGB scenario for MP formation, the blow-out of the bubble allows us to account for the fact that the material enriched by FG SNe is not incorporated into SG stars (Dalessandro et al. 2016; see also Calura et al. 2015)

Subsequently, as shown in the final panel of Figure 3.5, after a timescale of

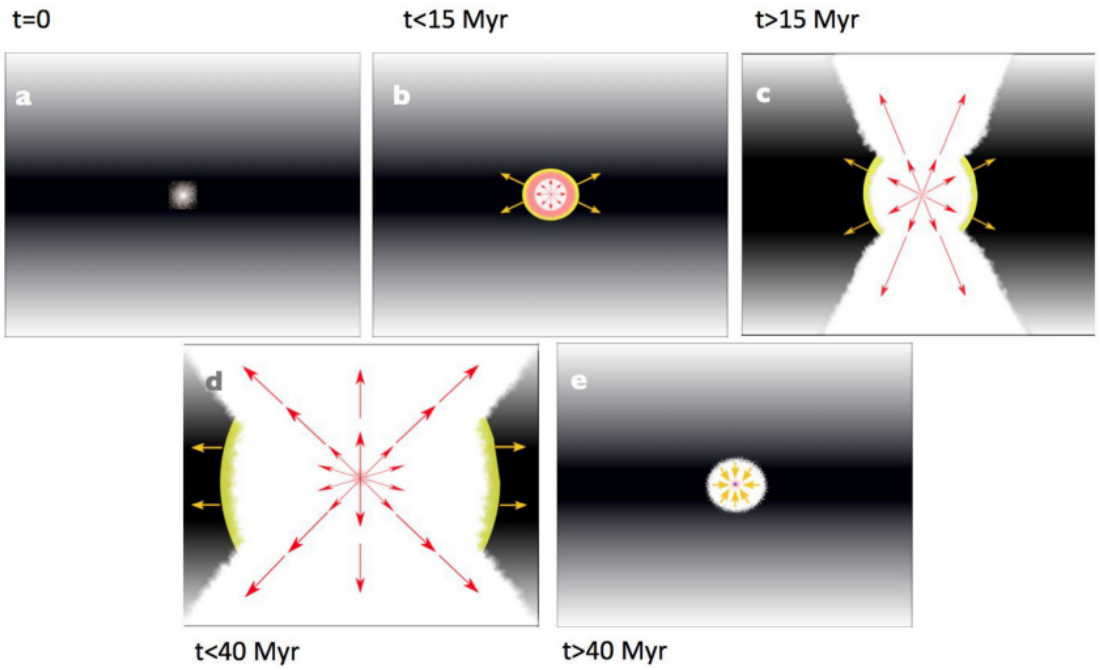

Figure 3.5. TSchematic illistration of a FG cluster embedded in the disk of a star forming, high redshift galaxy (D'Ercole et al. 2016). Times are indicative of the cluster age. *Panel (a)*: birth of the FG in the mid-plane of the stratified ISM (grey-scale) of the galactic disk. *Panel (b)*: beginning of the SN II explosions, with expansion of the bubble in the disk. The local gas swept up by the bubble is confined in a cool, dense, thin shell (yellow), while the free expanding wind powered by the SNe (red arrows) is thermalized (red area) by the reverse shock of the bubble. *Panel (c)*: the bubble expands beyond the disc scaleheight and the SN wind is lost into the circum-galactic medium. *Panel (d)*: the cavity in the disc expands as long as the SNe keep exploding. Depending on the parameters, it may still increase in size for a while after the SN activity, until its expansion velocity slows down to the velocity dispersion of the surrounding gas. *Panel (e)*: after the end of the SN II explosions, the disc matter closes up again onto the cluster. Depending on the bubble radius, there may be time, or not, to form an extreme SG from the super–AGB ejecta; then SF includes AGB matter partially diluted with the re-accreted disc gas.

the order of 25-30 Myr, corresponding to the lifetime of the least massive CC SN progenitor ($8\,M_\odot$) the CC-SNe cease and, the cluster can accrete material from the ISM while orbiting the galactic center. In particular, assuming that FG SNeII carved a substantial cavity in the external gas distribution, and the FG cluster moves along it, the system undergoes an asymmetric re-accretion of ISM gas from the side toward which the cluster is moving (D'Ercole et al. 2016) . It is noteworthy that the orbital motion of the cluster in this scenario is crucial for gas reaccretion, as previous studies have shown that the SG cannot form solely from AGB ejecta. The observed abundance pattern of light elements, indeed, wouldn't be replicated without a degree of dilution from pristine gas, unaffected by either FG SNe or AGB stars enrichment (see, e.g., D'Ercole et al. 2011; Bastian & Lardo 2015).

In particular, once the wind ram pressure of the superbubble shell equals the ISM pressure, the shell merges with the external ISM. Consequently, the bubble loses its initial structure and is considered a cavity in the disk, created by the feedback from massive FG stars. At this stage, the cavity reaches a defined radius known as the stalling radius (R_{eq}), marking the onset of ISM gas accretion, referred to as the infall time. The cavity then begins to refill with ISM gas at a velocity approximately matching the local sound speed.

Following D'Ercole et al. (2016), the stalling radius is computed as:

$$R_{\rm eq} = 4.143 \cdot 10^3 \left(\frac{L_{41}}{n_0 (\sigma_{\rm pg,6} + v_{\rm pg,6})^2 V_{\rm w,8}} \right)^{1/2} \text{pc} \tag{3.9}$$

Here, L_{41} is the mechanical luminosity of FG SNe in units of 10^{41} erg/s, $V_{\rm w,8}$ is the velocity of the SN ejecta in units of 10^8 cm/s, $\sigma_{\rm pg,6}$ and $v_{\rm pg,6}$ are the isothermal sound speed and the velocity of the pristine gas relative to the globular cluster (both in units of 10^6 cm/s), and n_0 is the ISM number density in cm^{-3}, here expressed as $\sim \rho_{pg}/m_p$ (with m_p proton mass).

The infall time is calculated as:

$$t_{\rm inf} = t_{\rm SN} + \frac{R_{\rm eq}}{\sigma_{\rm pg} + \nu_{\rm pg}} \tag{3.10}$$

where $t_{\rm SN} \approx 30$ Myr is the time at which SN II explosions are assumed to cease.

Now, let us define the simulation setup, detailed by Calura et al. (2019), and the main simulation parameters, consistent with those of Yaghoobi et al. (2022).

The scenario just described is simulated under three different initial conditions using a customized version of the RAMSES code, resembling a "wind tunnel" experiment with time integration beginning at $t_{SN} \sim 30 Myr$. In this simulation, a 3D computational box with a side length of 50 pc, initially gas-free and containing the FG star cluster, starts undergoing infall from the pristine, uniform gas, entering from one of the boundaries and moving at a constant velocity parallel to the x-axis

(see Figure 3.6; the properties of the pristine gas are in Table 3.1). At some other time (that might be either before or after the time of the infall, depending on the cluster mass and geometry, see Yaghoobi et al. 2022) AGB stars start releasing their ejecta, that can mix with the pristine gas and form SG stars.

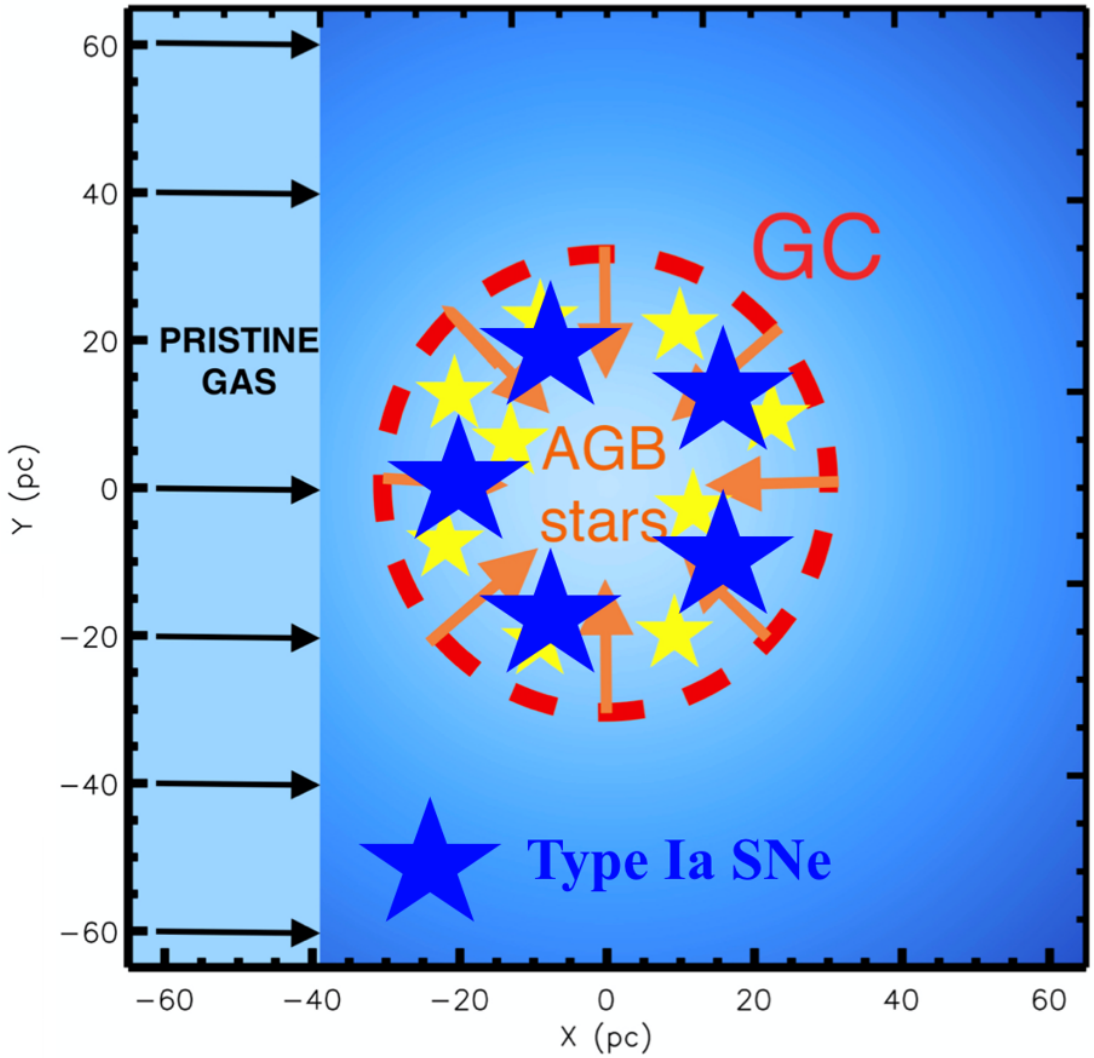

Figure 3.6. A schematic description of the setup of the Calura et al. (2019) setup which well describes our scenario. At the initial stages of our simulation, approximately corresponding to $t_{SN} \approx 30$ Myr after the formation of the cluster, the ejecta from first-generation AGB stars are released, allowing the formation of second-generation stars from this enriched gas. After CC-SNe stop exploding, a uniform pristine gas distribution, sharing the chemical composition with the FG stars, enters the computational box from one the left boundary, parallel to the x-axis.

Together with stellar feedback and radiative cooling, along with the self-gravity of the gas, are considered, taking into account the chemical composition of the

stellar ejecta and of newly formed stars. Figure 3.6 schematically illustrates the aforementioned setup. Finally, SNeIa feedback, a unique aspect of this work, is implemented to understand its role in stellar formation and its role in the chemical enrichment of SG stars.

Parameter	Description	Adopted values
$M_{\rm FG}$	Stellar mass of the FG	$10^5; 10^6 M_\odot$
$r_{\rm plum}$	Plummer radius of FG stellar distribution	3 pc
$P_{\rm pg}$	Density of the pristine gas	$10^{-24}; 10^{-23}$ g/cm^3
$V_{\rm pg}$	Pristine gas velocity relative to the cluster	$2 \cdot 10^6$ cm/s
$Z_{\rm pg}$	Metallicity of the pristine gas	0.001
$X_{\rm Fe}$	Iron mass fraction of the pristine gas	$3.77 \cdot 10^{-5}$
$X_{\rm He}$	Helium mass fraction of the pristine gas	0.246
$T_{\rm pg}$	Temperature of the pristine gas	10^4 K
$T_{\rm floor}$	Minimum temperature	10^3 K

Table 3.1. Initial conditions parameters of the simulations.

The three simulation vary in two crucial parameters: the pristine and infall gas density (10^{24} or 10^{23} g/cm^3), and the stellar mass of the first generation (10^5 or 10^6 M$_\odot$). The parameters related to the initial conditions of the models are shown in Table 3.1 while the infall times are estimated by means of Eq. 3.9 and 3.10 (Table 3.2). The time reference used in this thesis for the analysis of the three models is 31.3 Myr from the birth of the FG, meaning that every referenced time should be understood as t + 31.3 Myr from the cluster's formation. In Table 3.2, we also report $t_{\rm SNeIa}$, the starting time, in our time reference, of the DTD of SNeIa explosions.

Simulation	M$_{\rm FG}$ [M$_\odot$]	$\rho_{\rm pg}$ [g/cm^3]	Req [pc]	t_0 [Myr]	$t_{\rm inf}$ [Myr]	$t_{\rm AGB}$ [Myr]	$t_{\rm SNeIa}$[Myr]
M5-INFALL24	10^5	10^{-24}	131	34.3	3	7.7	7.7
M6-INFALL24	10^6	10^{-24}	414	43.5	12.2	7.7	7.7
M6-INFALL23	10^6	10^{-23}	131	34.3	3	7.7	7.7

Table 3.2. Main simulation parameters. Here $M_{\rm FG}$ is the mass of the cluster, $\rho_{\rm pg}$ is the ambient density, the stalling radius $R_{\rm eq}$ and the time at which the infall starts t_0 are computed by means of equations 3.9 and 3.10, respectively. The infall time in the time reference frame assumed in this study is $t_{\rm inf}$ and is given by $t_0 - 31.3$ Myr. $t_{\rm AGB}$, calculated as $t_{\rm inf}$, represents the time at which material injection by intermediate mass FG stars in AGB phase starts. In the last column $t_{\rm SNeIa}$ represents the starting time of the DTD of SNeIa explosions in our time reference.

Chapter 4

Results

In this Chapter, we present the results of the analysis of three simulated models representing an astrophysical scenario in which a globular cluster orbits with a constant rotational velocity around the centre of a high-redshift galaxy.

The simulation tracks the temporal evolution of a 50 pc box filled with a homogeneous and isothermal gas (*pristine gas*) after the Type II Supernovae (SNII) explosions of massive first generation (FG) stars. This box, containing a Plummer sphere potential with a mass equal to that of the FG population, is enriched with material from stars in the AGB phase, experiences the infall of gas from a homogeneous and isothermal distribution, and includes also Type Ia Supernovae (SNeIa) explosions with the delay time distribution of Greggio 2005, a unique aspect of this analysis.

The three simulation results presented here differ in two key variables: infall gas density and the stellar mass of the first generation. In Table 3.2, we summarize the main simulation parameters of each model.

We will begin by describing the evolution of gas in its hydrodynamic variables and the spatial distribution of second generation (SG) stars. Subsequently, we will explore the mass distribution of the simulated stars and their chemical abundances and compare the different star formation rates (SFR) among the three simulations. Finally, we will make a comparison with some observational data and Yaghoobi et al. (2022) work.

4.1 Model M5-Infall24

This model has an initial cluster mass $M_{\rm FG} = 10^5\,{\rm M}_\odot$ and pristine gas density $\rho_{\rm pg} = 10^{-24}\,{\rm g/\,cm^3}$ and its accretion starts with the injection of infall gas material at $t_{\rm inf} = 3$ Myr, followed by the enriched AGB stars ejected material at $t_{AGB} = 7.7$ Myr.

4.1.1 Dynamical evolution of the gas and SG stars spatial distribution

In Figure 4.1 we show four snapshots of two-dimensional density (*left column*), pressure (normalized to Boltzmann constant) (*middle column*) and temperature (*right column*) maps. The maps were created by selecting all the grids located on a slice centered in the middle of the computational box. This slice is perpendicular to the z-axis and passes through the midpoint of the computational volume. In Figure 4.2, we display the surface stellar mass density at the same time values. In both figures, the four evolutionary times are 18 Myr, 34 Myr, 46 Myr, 55 Myr.

At $t = 18$ Myr, the gas accreted by the system, fallen into the potential well, is found condensed at the center of the system with $\rho > 10^{-22}$ g/cm^3, is cool (recall $T_{floor} = 10^3$ K, the lower temperature limit of the system), and at high pressure (P/k$_b$ $> 10^6$ K/cm^3). A feature noticeable from the maps is a coneshaped gas structure formed in the direction of the gas motion. Due to its high velocity, after passing through the cluster core, the gas is re-directed back towards the centre through a tail of denser cold gas. Additionally, when examining the maps of surface stellar density, it becomes evident that all stars are compactly formed in the central region in a quasi-spherical structure.

At a later time ($t = 34$ Myr), in the second row of the gas maps, a recent SN Ia close to the center has increased the system's energy, leading to high temperature and high pressure throughout the entire box. In the density map, we observe a cavity filled with gas which is both warm and with high pressure (P/k$_b$ $> 10^7$ K/cm^3). Similar to the previous snapshot, the central region with the highest density ($\rho \simeq 10^{-(20-21)}$ g/cm^3) is completely cooled with a more compact appearance than before . Additionally, the recent gas activity resulting from the SN explosion, combined with the high-speed motion of infalling gas, creates an even broader cone-shaped structure with symmetric features.

At t=46 Myr, the gas setup is similar to the first set of snapshots, with a slightly sharper cone. Despite the energy injection from SNeIa, efficient cooling still allows the system to collect cold gas in the centre. What is noticeable in Figure 4.2, however, is an almost negligible variation in the spatial distribution of SG stars, with no significant changes in star formation.

In the last set of maps at t=55 Myr, supernova explosions have depleted the gas from most of the volume. In the meantime, some gas has started to accumulate in the centre again. On the left side of the box, we find a homogeneous and nearly isothermal distribution of infalling gas, and in the upper right, there is a tail of cold gas channeling towards the center of the system. At the system's center, we have a pressure comparable to the first and third snapshots, but with higher temperatures ($T > 10^4$K) and lower densities ($\rho < 10^{-22}$ g/cm^3). This reveals that, compared to earlier times, the rate of SNeIa, with its heating effect in the central region of the cluster, is capable of slowing down and halting the star formation within the system. The similarity in surface stellar mass density between the last two snapshots (second row) seems to confirm the significant role of SNeIa in the system's SFR.

In section 4.4, where we examine the temporal changes in the mass of second-generation stars and the Star Formation History (SFH) of our system, we will further explore these aspects.

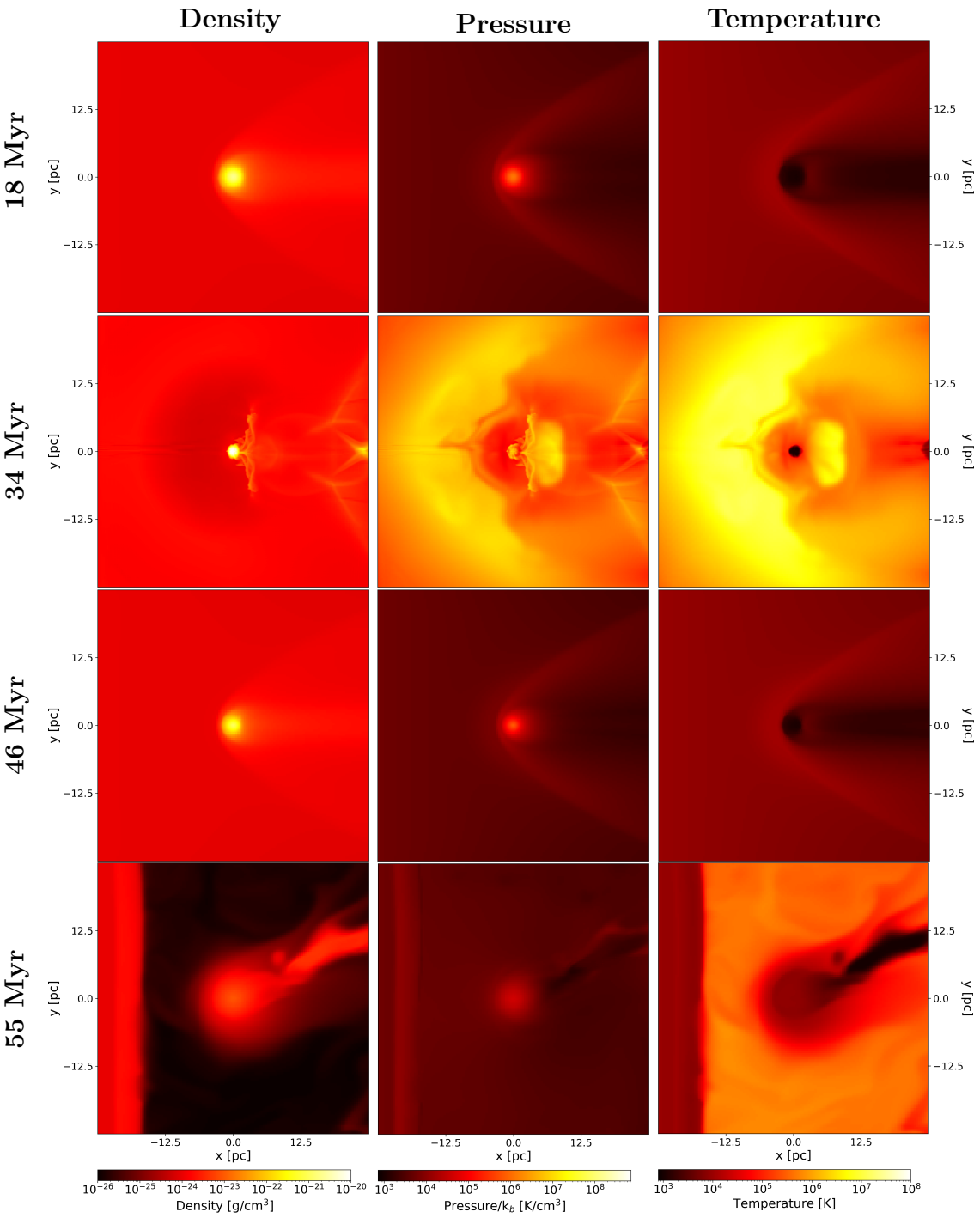

Figure 4.1. Two-dimensional slice maps of the gas density (*left-hand panels*), pressure (*middle panels*) and temperature (*right-hand panels*) in the x-y plane are presented at various stages of evolution for the M5-Infall24 model, a low mass ($10^5 M_\odot$) and low density ($\rho = 10^{-24}\,\mathrm{g/cm^3}$) simulation. The infall gas, as implemented, enters from the left side of the computational box. The evolutionary times are indicated on the left of each set of panels. From top to bottom: $t =$ 18, 34, 46, 55 Myr.

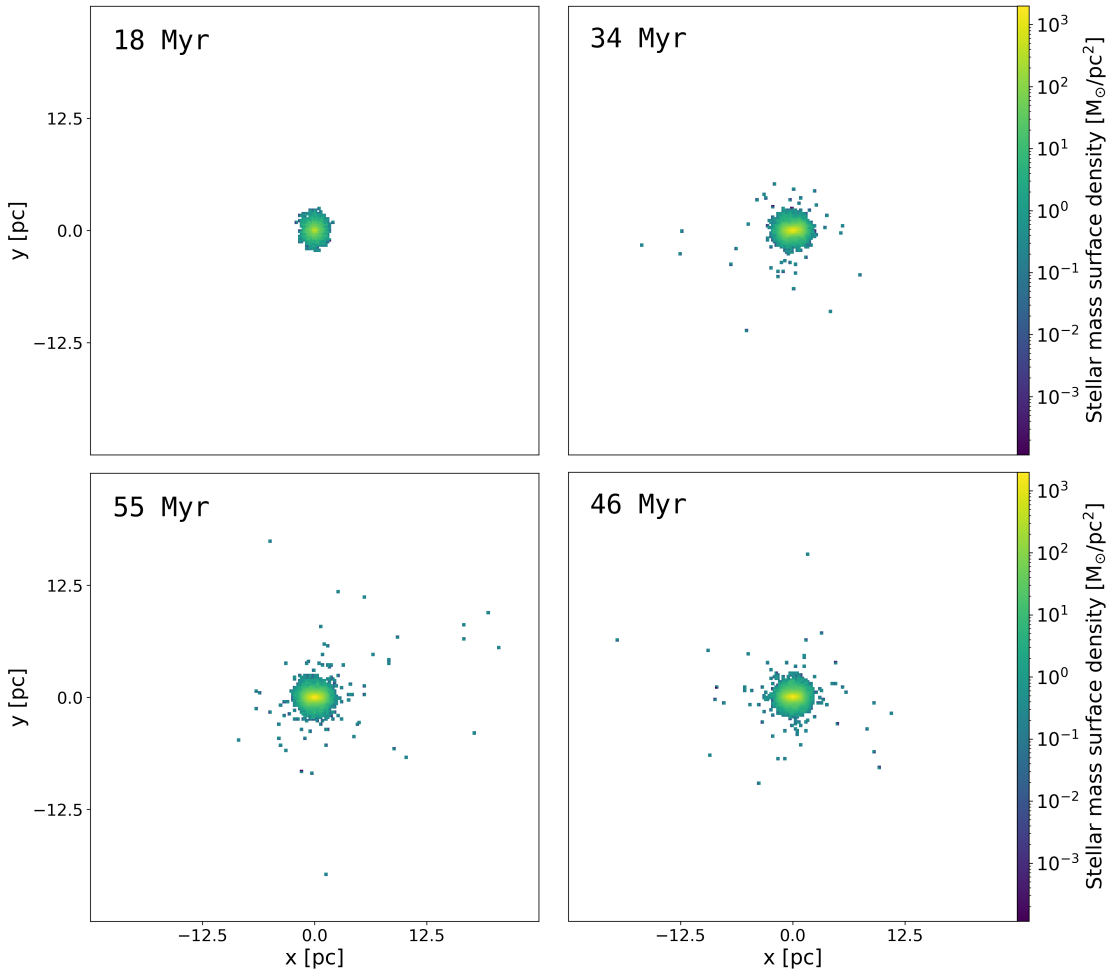

Figure 4.2. Two-dimensional projection maps of the surface stellar density in the x-y plane are presented at various stages of evolution for the M5-Infall24 model, a low mass ($10^5 M_\odot$) and low density ($\rho = 10^{-24}\,\mathrm{g/\,cm^3}$) simulation. Clockwise, from top to bottom: t = 18, 34, 46, 55 Myr.

4.1.2 Stellar abundances

4.1.2.1 Helium mass fraction Y

In the *left column* of Figure 4.3, we show the density profiles for the FG (dashed lines) and for the second generation (SG) at different evolutionary times (t = 18 Myr, 34 Myr, 46 Myr and 55 Myr). The SG profiles include both the overall profile (black solid lines) and profiles calculated for different ranges of the helium mass fraction Y. These quantities were computed with the origin set at the system's center of mass. In the right column, on the other hand, we plot the mass distribution function of Y. The dashed black line represents the Y of pristine gas and FG stars (refer to the pristine gas initial conditions Table 3.1), the solid black line

shows the normalized cumulative mass as a function of Y, and the term σ at the bottom left indicates the standard deviation calculated based on the histogram bin centers. In Figure 4.4, additionally, we present a slice colormap representing the SG stars in the Y-birthtime plane. In this analysis, "birthtime" refers to the moment in time, measured from the start of the simulation, when the SG star is born.

At 18 Myr, the material accumulated in the central region, composed by a mix of pristine gas and AGB ejecta, formed a very compact (r<2pc) SG component, with densities exceeding those of the Plummer sphere of the FG. This component is mainly constituted of He-rich stars (Y $\simeq$ 0.35).

At 34 Myr, the SG stars have further concentrated in the central regions, reaching the maximum stellar density for this model ($\rho \simeq 10^{-18}$ g/cm^3). Compared to the previous timeframe, we note a subtle broadening in the mass distribution across Y and an off-center spatial distribution of these stars. In particular, from the density plot, it is possible to observe a more widely distributed second population with a slightly lower helium mass fraction (0.30 < Y < 0.33). The colormap in Figure 4.4 shows a star formation hiatus between this time step and the previous one, attributed to the influence of SNeIa explosions and a discontinuity in the Y distribution, evident in the second peak of the histogram (Figure 4.3) at Y < 0.35. Additionally, the decreasing trend over time in the helium mass fraction is attributed to the decreasing AGB yield over time while while the spread of Y at the given time suggests mixing of AGB ejecta with infall gas. Lastly, it's interesting to point out that at this specific moment, the graph in Figure 4.4 corresponds to another hiatus in star formation. As discussed earlier in connection with the gas map at the same timestep, these pauses are linked to the occurrences of SNeIa explosions.

At a later time (t=46 Myr), the observed trend from the previous time step persists. The He-rich stars expand spatially, forming a flatter curve, and the star formation has slightly broadened the mass distribution in Y. The new population with a lower helium mass fraction continues to increase, forming compactly in the central region.

At the final time, t=55 Myr, there is a condensation of the He-intermediate stellar population (0.30 < Y < 0.33) in the central regions, exceeding the density of FG stars for the innermost radii. The evolution of Y suggests that during this time interval, star formation is resuming after a previous interruption. As evident, indeed, from the histogram (Figure 4.3, right column) and the map (Figure 4.4), there is a substantial He-intermediate star formation with a peak at Y $\simeq$ 0.32.

In conclusion, the He-rich group is the dominant population in the second generation of stars, created out of FG AGB stellar ejecta. We observe, indeed, an inefficient mixing of gas from AGB ejecta with infall gas, reflected in a gradual

decrease in Y over time. The injection of energy from SNeIa significantly alters SFH and stellar distribution, manifesting in lower compactness in central regions (roughly 1 dex) and a broader distribution in outer regions compared to scenarios without SNeIa (see Yaghoobi et al. 2022). Furthermore, the intermittent halting of star formation at various time intervals (see Figure 4.4) facilitates the emergence of multiple populations with distinct helium mass fractions.

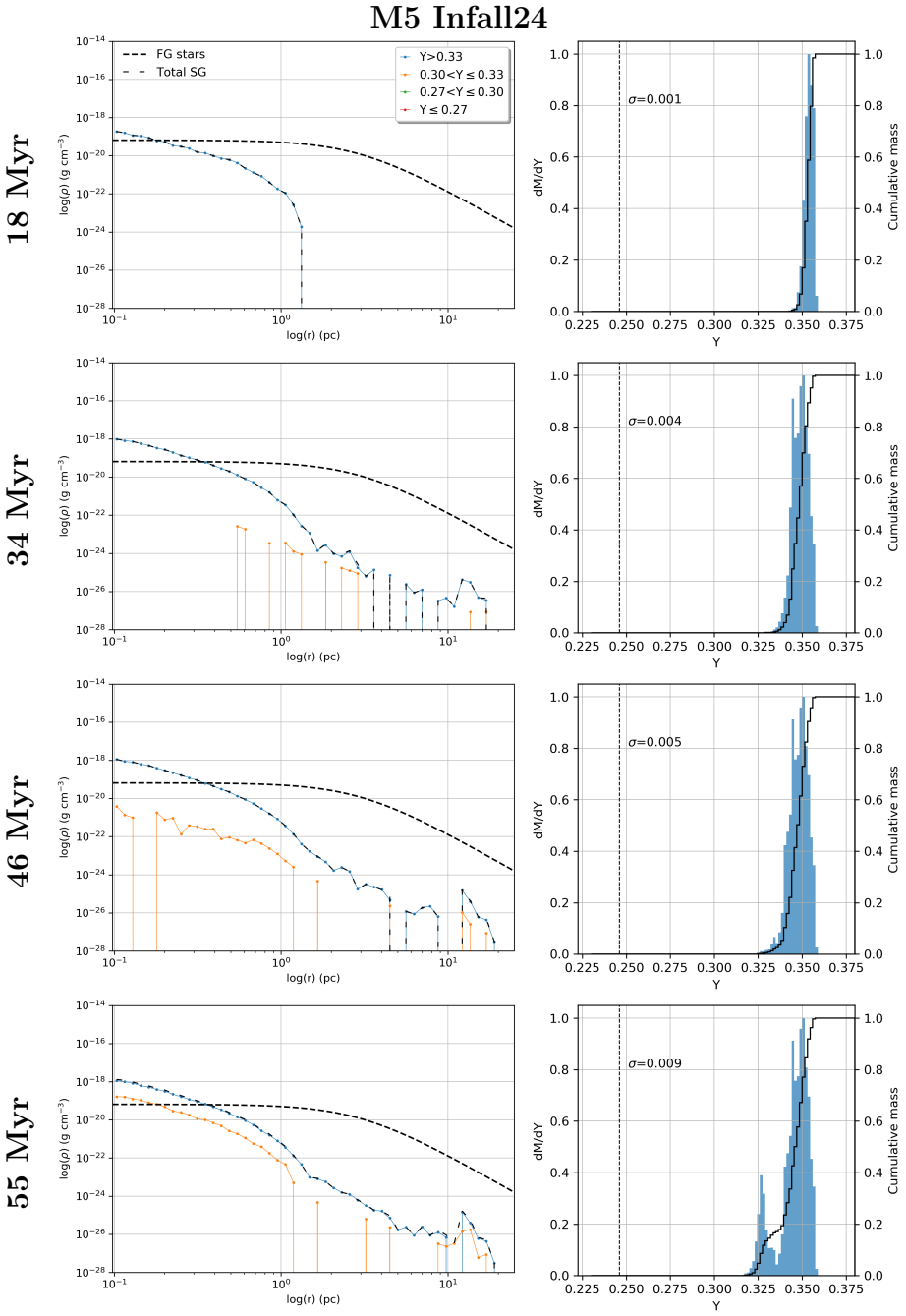

Figure 4.3. *Left column*: total density profile of SG stars and density profiles of SG stars categorized by helium mass fraction (Y) bins for the low-mass ($10^5 M_\odot$) and low-density ($\rho = 10^{-24}\,\mathrm{g/cm^3}$) model. The density profile of FG stars is also included for reference, represented by a black dashed line. *Right column*: mass distribution of Y in SG stars. These distributions are obtained by summing the masses of stars within each Y bin, and then normalizing each distribution to its maximum value. The black dashed vertical lines denote the pristine gas composition while the solid black line represents the normalized cumulative mass as a function of Y. In each panel we also report the Y spread (σ), computed as the standard deviation of the distribution. The evolutionary times are indicated on the left of each set of panels. From top to bottom: t = 18, 34, 46, 55 Myr.

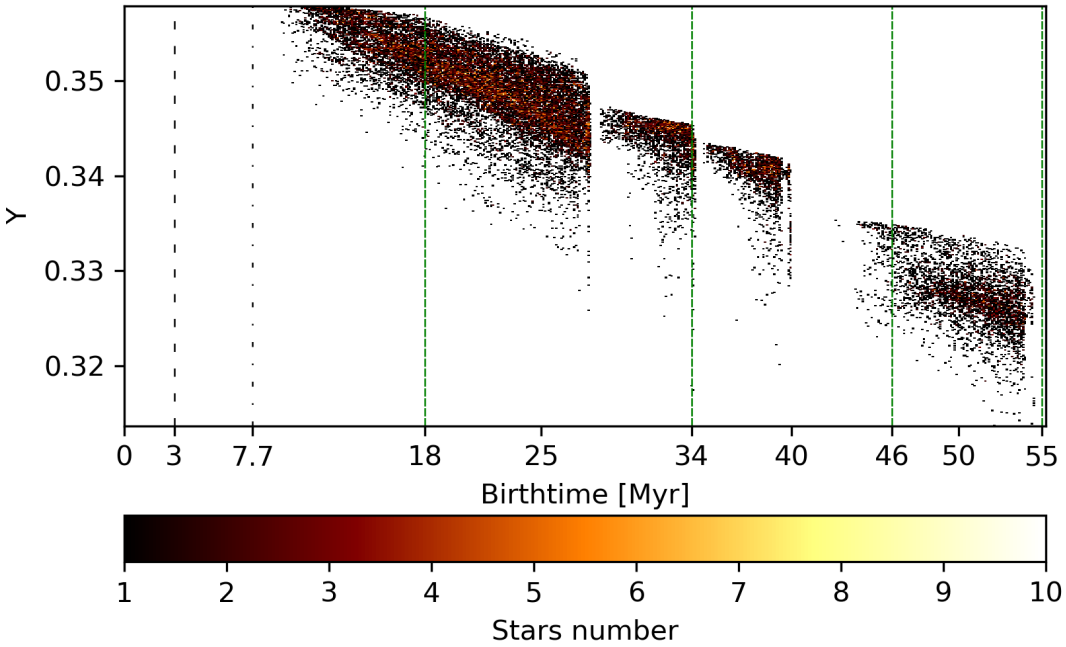

Figure 4.4. Helium mass fraction (Y) and stars birthtime 512x512 colormap for the M5-Infall24 model. The color scale indicates the number of SG stars. The green dashed vertical lines represent the reported evolutionary times (18, 34, 46, 55 Myr). The black vertical lines mark the time at which the infalling gas (dashed line) crosses the center of the cluster and the onset of the injection of AGB ejecta (dash dotted line). In this scenario $t_{\rm inf} = 3\,$Myr and $t_{\rm AGB} = 7.7\,$Myr (see Table 3.2).

4.1.2.2 Iron-to-hydrogen abundance ratio [Fe/H]

In Figure 4.5, we present the same configuration as shown in Figure 4.3, but this time in terms of the iron-to-hydrogen abundance ratio [Fe/H] rather than the helium mass fraction Y.

Similar to Y, the mass distribution of [Fe/H] will vary based on AGB ejecta[1] and dilution from infalling pristine gas. Additionally, in this analysis, the more pronounced contribution of SNeIa explosions in enriching the gas with iron will become evident.

At the first timestep (t =18 Myr), we observe a metal-poor population ([Fe/H]<-1.5) that shares the same distribution as the He-rich population discussed earlier. Since this population is primarily originated from material expelled by AGB stars (as explained in the previous paragraph), it is reasonable to assume that the enriched material ejected by SNeIa is negligible at this stage. Therefore, this chemical

[1]It should be noted that the helium yield from AGB stars decreases with increasing stellar mass, consequently leading to a decrease in the [Fe/H] of the ejecta throughout the system's evolution. Nevertheless, this variation is nearly negligible within the time interval under consideration.

composition is likely to reflect the dilution of material expelled by AGB stars with pristine gas.

At 34 Myr, the metal-poor population increases in number, displaying higher density in central areas and a more widespread spatial distribution. Additionally, a group of stars with higher iron content (-1.3<[Fe/H]<-1.5) has compactly formed at the center of the cluster. This variation in the stellar abundances of the system is also evident in the right column with a wider histogram. In this case, the observed [Fe/H] values are linked to contamination from SNeIa, although the impact remains relatively limited.

At the next time step (t=46 Myr), we observe a broader spatial distribution for the metal-intermediate population, resulting from decentralized star formation, as seen in the surface density maps of stars (Fig. 2). This decentralization is attributed to the previous supernova explosions that have swept away the gas. The increased number of this population is evident in the right column, indicating a rise in the mass distribution of [Fe/H] with iron abundances greater than -1.5 dex.

In the last evolutionary time, at 55 Myr, not much differences can be seen in the graphs if compared with the previous ones. The [Fe/H] mass distribution remains practically unchanged, given the reduced star formation, and stars generated during this period make a negligible impact.

Across all selected evolutionary periods, SG stars exhibit dominance within the central 0.4 pc, while, in outer regions, the majority of stars belong to the FG, consistent with empirical observations (Lardo et al. 2011; Dalessandro et al. 2019). Although our findings share similarities with those of Yaghoobi et al. (2022), substantial distinctions emerge upon closer examination. Notably, the total stellar density of the SG in the central region is nearly one order of magnitude lower than in their study. Additionally, a significant dissimilarity is evident in the helium enrichment of SG stars. Our analysis reveals that SG stars with an extreme helium composition prevail at all radii, in contrast to Yaghoobi et al. (2022), where this population is concentrated in the central part of the system without dominating in the outskirts. Furthermore, while both simulations showcase a He-rich SG stars population, our study reveals distinct peaks in Y during the star formation process. Finally, the total mass of SG stars in this model amounts to $1.1 \cdot 10^3 M_\odot$, representing approximately a $\sim$56% reduction in mass compared to the scenario without SNeIa after 71 Myr. In Section 4.4, we will discuss the viability of comparing the two mass values despite the age difference in the two simulations.

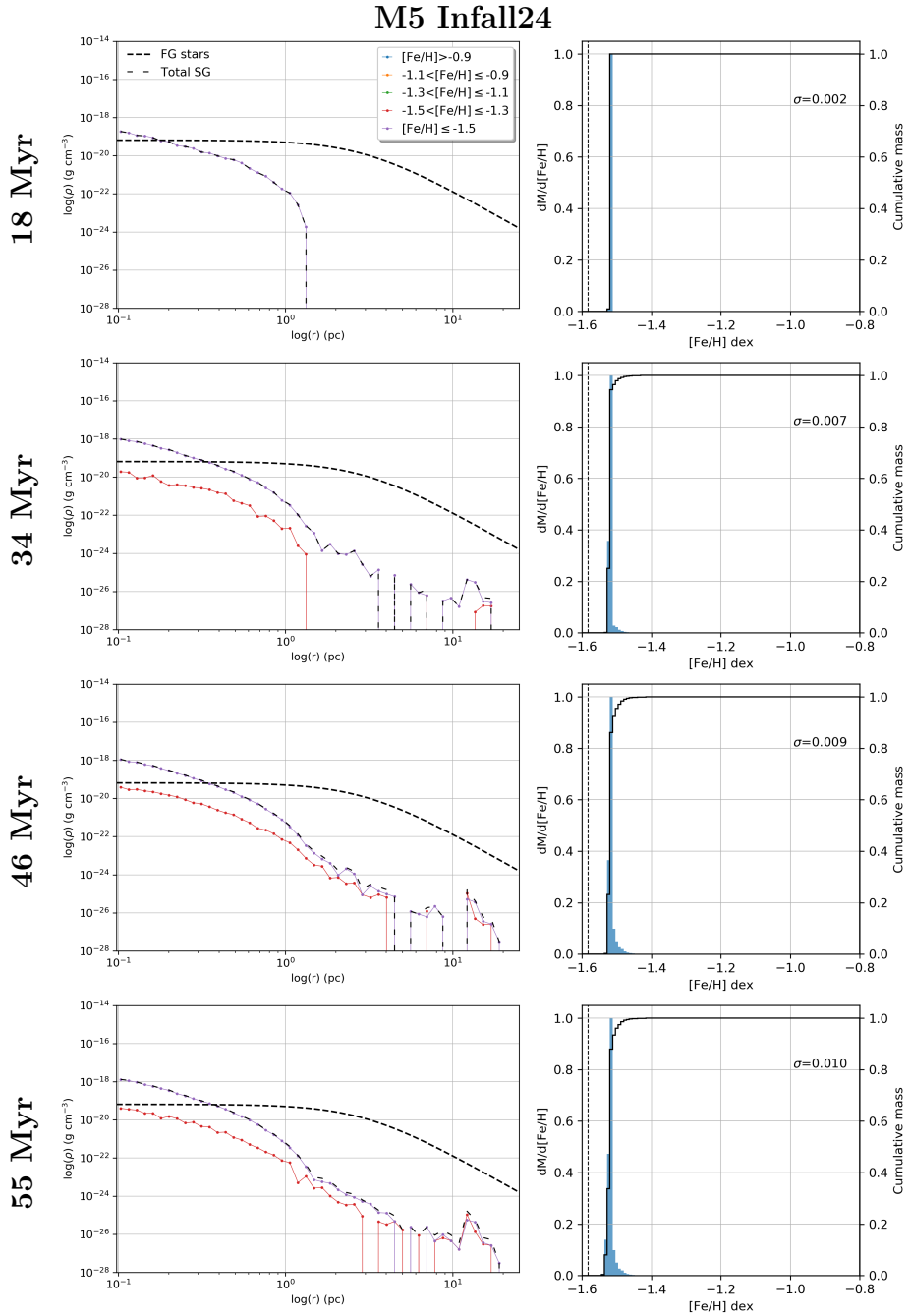

Figure 4.5. *Left column*: total density profile of SG stars and density profiles of SG stars categorized by [Fe/H] ratio (Y) bins for the low-mass ($10^5 M_\odot$) and low-density ($\rho = 10^{-24}\,\mathrm{g/cm^3}$) model. The density profile of FG stars is also included for reference, represented by a black dashed line. *Right column*: mass distribution of [Fe/H] in SG stars. These distributions are obtained by summing the masses of stars within each [Fe/H] bin, and then normalizing each distribution to its maximum value. The black dashed vertical lines denote the pristine gas composition while the solid black line represents the normalized cumulative mass as a function of [Fe/H]. In each panel we also report the [Fe/H] spread (σ), computed as the standard deviation of the distribution. The evolutionary times are indicated on the left of each set of panels. From top to bottom: t = 18, 34, 46, 55 Myr.

4.2 Model M6-Infall24

Here, we present an analysis of a cluster characterized by a FG with a mass ten times greater ($10^6\,M_\odot$) than that analyzed in Section 4.1 and the same pristine gas density ($\rho_{\rm pg} = 10^{-24}\,{\rm g/\,cm^3}$). In contrast to the less massive FG of the preceding section, the start of pristine gas infall is delayed in this case. By applying equations (3.9) and (3.10), we determine that the infall begins at $t_{\rm inf} = 12.2$ Myr, with a 4.5 Myr delay after the onset of AGB ejecta at $t_{\rm AGB} = 7.7$ Myr.

In this scenario, the cluster's gravitational potential well is deeper than the previous simulation. As a result, compared to the earlier system, both ram pressure and the energy injection from SNeIa are ineffective in preventing the cluster from retaining a significant amount of gas. This effect contributes to a more conspicuous star formation. Furthermore, the resultant iron contamination in SG stellar abundances due to SNeIa events is notably more significant in this scenario.

4.2.1 Dynamical evolution of the gas and SG stars spatial distribution

In the next two figures, we present density, pressure normalized to the Boltzmann constant, and temperature maps (Figure 4.6), along with the spatial distribution of SG stars (Figure 4.7) from our simulation, which includes a more massive FG cluster in the x-y plane computed at 17, 34, 46, and 55 Myr.

In the first row of panels in Figure 4.6, at 17 Myr, the gas maps reveal a central compact gas region with densities higher by an order of magnitude with respect to the previous model (ρ>10^{-21}g/cm^3, see Figure 4.1). Here the pressures are high (P/k$_b$>10^7 K/cm^3), and temperatures have already reached the simulation's minimum (T=T$_{floor}$). This feature will be present at all four time steps. The plot illustrates infalling gas in an oblique beam, creating cavities of hot gas on the top and bottom right corners of the box. The central gas beam suggests the development of an accretion tail, transporting cold gas towards the central regions. Turning attention to the stellar component, an elongated structure along the x-axis (aligning with the direction of motion) is observed, characterized by a surface density of over $10^5\,M_\odot/\,{\rm pc}^2$ at the very center of the box (r<1pc) surrounded by a more diffuse distribution of stars.

At 34 Myr, just like in the previous model, the high temperatures and pressures of the gas (T>10^6K; P/k$_b$> 10^6K/cm^3) along with its lower density ($\rho < \rho_{pg}$) reflect a recent injection of SNeIa energy thermalized by the system. Furthermore, the density map reveals a cold and dense narrow tail along the x-axis and a circular shape structure in central regions. In the surface stellar mass density map, a significant increase in star formation is evident compared to the previous timestep,

both in the central and off-center regions, with newborn stars also present along the tail.

At the next timestep (t=46 Myr), the gas in most of the computational volume has low density, low pressure, and high temperature. On the left side of the box, there is a column of uniform and isothermal infalling gas.

At 55 Myr, minimal differences are observed compared to the previous timestep both in gas evolution and stellar mass surface density, primarily due to the reduced SFR and, consequently, the almost insignificant rise in the overall mass of SG stars during this period.

In summary, over the entire simulation duration, the gas has evolved similarly to the lower-mass case. Despite the slightly different model analysis, the density value contributes similarly to ram pressure, leading to a compact star formation in central regions and a more dispersed distribution in the outskirts. On the other hand, the different mass of first-generation stars facilitated higher gas density in central areas, promoting significant star formation.

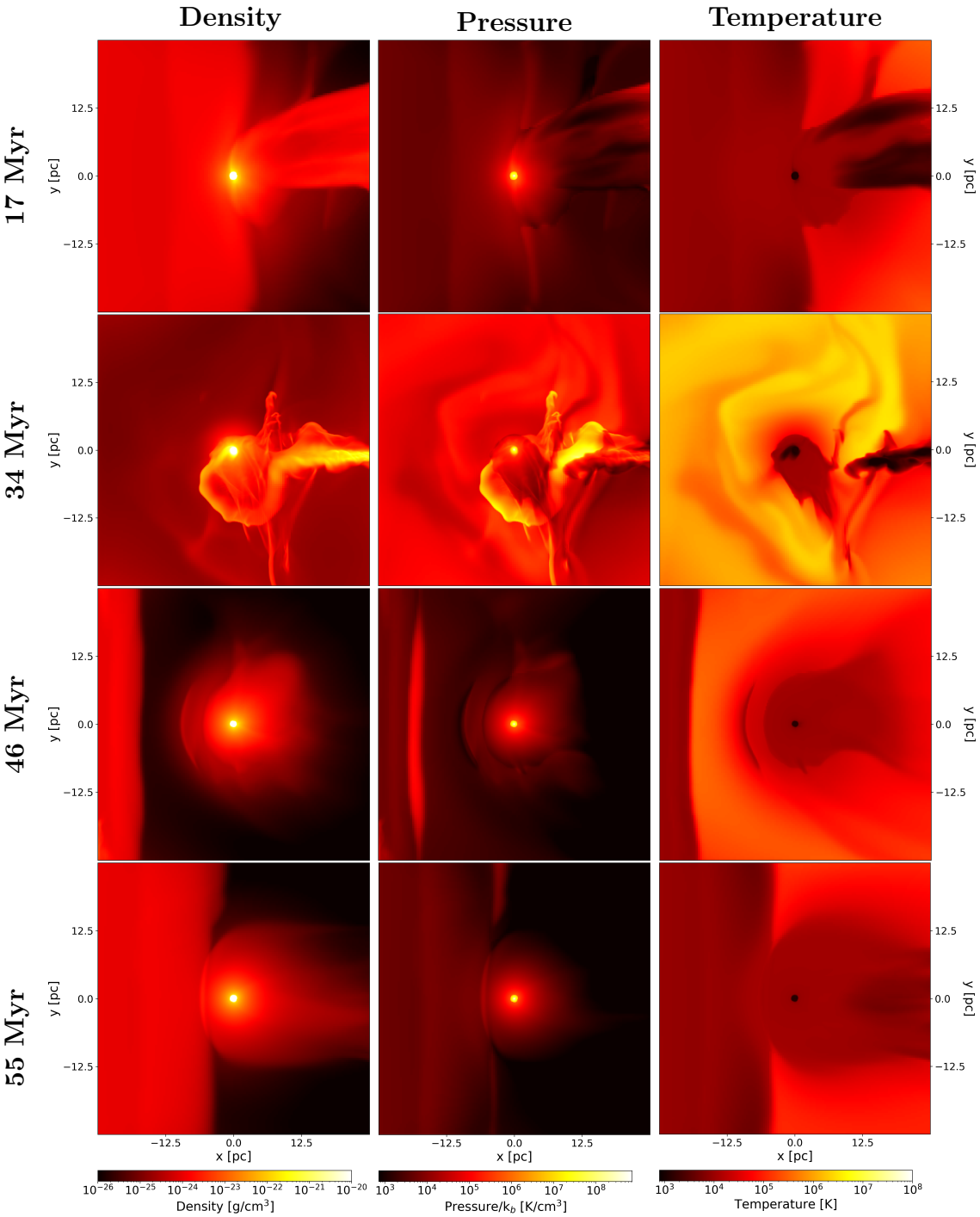

Figure 4.6. Two-dimensional slice maps of the gas density (*left-hand panels*), pressure (*middle panels*) and temperature (*right-hand panels*) in the x-y plane are presented at various stages of evolution for the M6-Infall24 model, a high mass ($10^6 M_\odot$) and low density ($\rho = 10^{-24}\,\mathrm{g/cm^3}$) simulation. The infall gas, as implemented, enters from the left side of the computational box. The evolutionary times are indicated on the left of each set of panels. From top to bottom: $t =$ 17, 34, 46, 55 Myr.

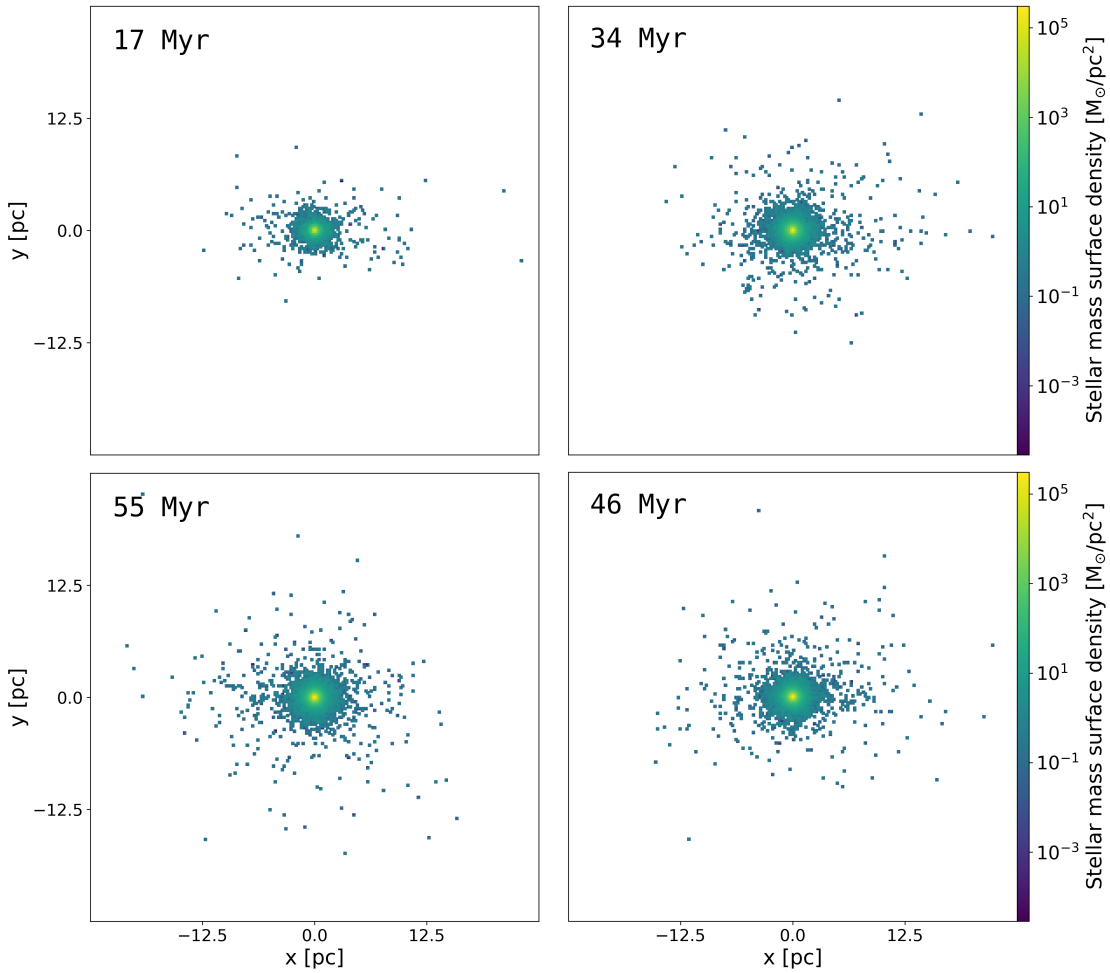

Figure 4.7. Two-dimensional projection maps of the surface stellar density in the x-y plane are presented at various stages of evolution for the M6-Infall24 model, a high mass ($10^6 M_\odot$) and low density ($\rho = 10^{-24}$ g/ cm^3) simulation. Clockwise, from top to bottom: t = 17, 34, 46, 55 Myr.

4.2.2 Stellar abundances

4.2.2.1 Helium mass fraction Y

In Figure 4.8 we plot the density profiles of SG, both total and for various helium composition, together with the Y mass distributions for the high-mass low-density model (M6-Infall24), at different evolutionary times. As in the previous case, the density profiles have been computed in a reference frame with the origin placed at the centre of the computational grid. In Figure 4.9, additionally, we present a colormap representing the number of SG stars in the Y-birthtime plane.

At 17 Myr, the total density of SG stars exhibits a peak in the central region, exceeding the density of FG stars within a radius of 0.2 pc (r $<$ 0.2 pc). The trend of

this curve aligns with that of He-rich stars up to a radius of 1 pc while beyond this radius, populations with lower helium abundance ($0.30<Y\leq0.33$; $0.27<Y\leq0.30$) become significant. Observing the mass distribution of Y, it becomes evident that He-rich stars dominate the total stellar population in mass, exhibiting a peak corresponding to approximately half of the system's mass at $Y>0.35$. Similar to the lower-mass case (M5-Infall24), we see a dominance of newborn He-enhanced stars ($Y>0.35$). However, in this scenario, the deeper potential well appears to have allowed for greater dilution of infalling gas, creating a less compact population with distinct peaks in helium.

In the next timeframe, t = 34 Myr, the density peak of He-rich stars reaches its maximum at the center of the box, approximately at a density $\rho=10^{-16}$ g/cm^3. A similar concentration towards the center is also observed for stars with helium abundance in the range $0.30<Y<0.33$, surpassing ($\rho= 10^{-17}$g/cm^3) the density of the first-generation stellar population at r<0.1pc and dominating the density in the region of 0.8 pc<r<1.1 pc. Meanwhile, the population with $0.27<Y<0.30$ prevails in the outer regions of the box, specifically at r>1.2 pc, up to a radius of 10 pc where, beyond that distance, we find a peak of He-rich stars. Lastly, a smaller group with lower helium abundance ($Y<0.27$) has emerged at a distance beyond 8 pc. The Y mass distribution plot confirms the dominance of He-rich stars, showing multiple peaks at $Y>0.33$. However, differently from the previous timeframe, the less helium-enhanced populations represent $\sim$20% of the system's mass. Notably, stars with $Y<0.30$ are negligible. Finally, as in the previous model, the decreasing trend in the helium mass fraction is attributed to the decreasing AGB yield over time. It is worth noting that, at this timestep, we observed a recent injection of energy from SNeIa in the gas maps. Figure 4.9 indicates a rapid increase in helium abundances in stars following this moment. This trend can be attributed to the accretion of AGB ejecta, occurring concurrently with the cessation of infall gas dilution swept away by the supernova.

At 46 Myr, we do not find any significant difference in the cluster density profile compared to the previous time step. What can be inferred from the graph on the right is a substantial formation of stars with $Y > 0.33$, while the contribution from less-enhanced SG stars seems almost negligible. The Y-birthime map supports this trend, showing small dispersions in Y during this time interval. As mentioned earlier, this could be attributed to the efficient injection of mass and energy from SNeIa.

At the last timestep, 55 Myr, there are no significant differences from the previous times. The formation of He-rich stars continues, evidenced by the peaks in the histogram at $Y>0.325$. There is increased star formation in the $0.30<Y<0.33$ range, seen as a "tail" in the Y mass distribution and in the central regions of the density profile, aligning closely with the most He-rich stars curve. Additionally,

there is a higher concentration of stars at $0.27<Y<0.30$ formed in the center, though their mass contribution remains negligible compared to the total system mass. The evolution of the stellar Y is displayed in Figure 4.9. We can observe a period of minimal dispersion in Y until $\sim$51 Myr, during which the material is primarily composed of AGB ejecta. Beyond this point, a dip is noticeable, indicating dilution of the AGB ejecta with infalling gas.

In conclusion, similarly to the previous model, the dominant population in the second generation of stars is the most He-rich group, mainly enriched by the activity of FG AGB stars. Over time, we observe a more efficient mixing of gas from AGB ejecta with infalling gas, reflected in a gradual decrease in Y and significant dips in Y dispersion. The injection of energy from SNeIa alters the evolution of the stellar population, manifesting in more compactness in central regions and a broader distribution in outer regions compared to scenarios without SNeIa (see Yaghoobi et al. 2022).

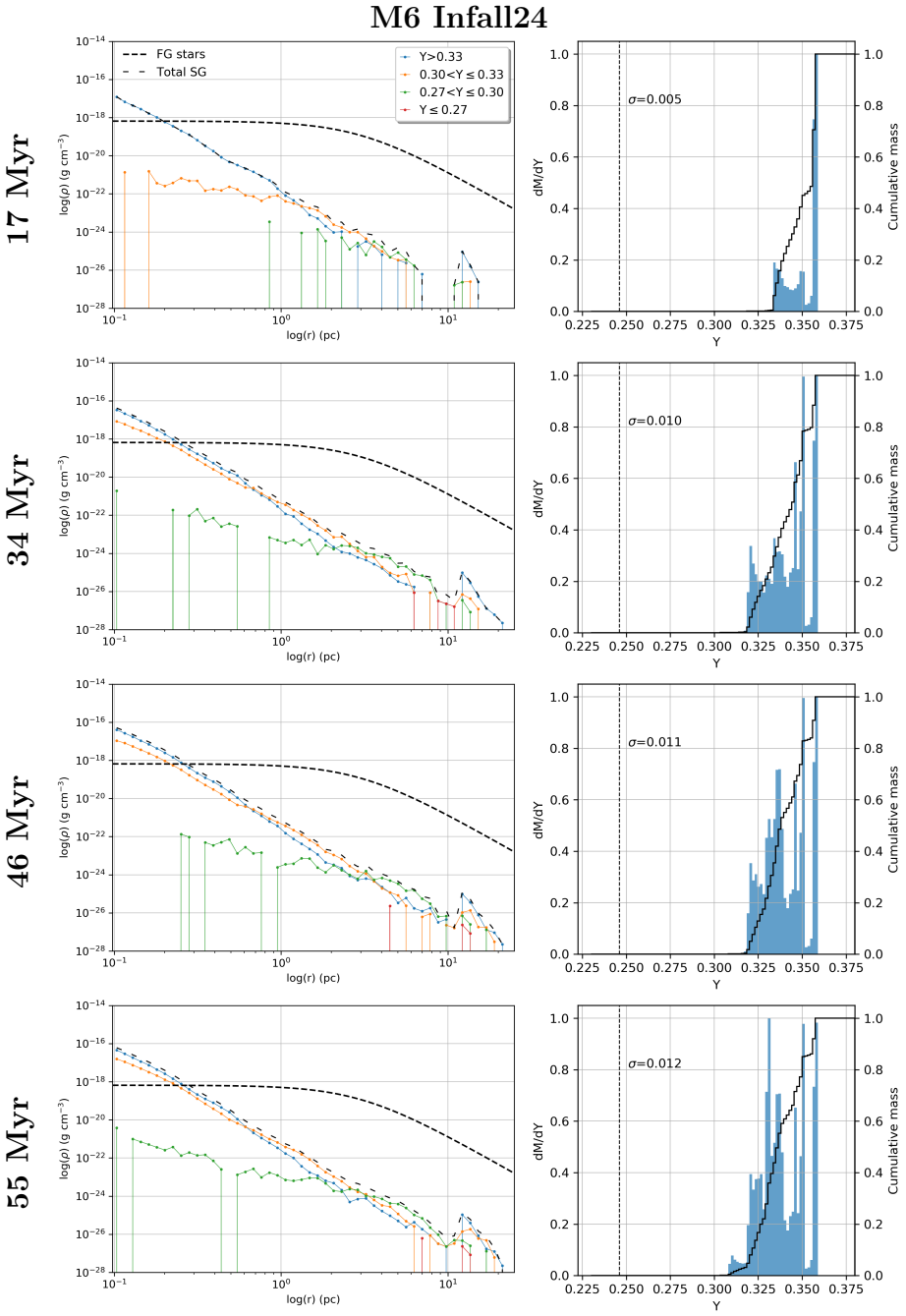

Figure 4.8. *Left column*: total density profile of SG stars and density profiles of SG stars categorized by helium mass fraction (Y) bins for the high-mass ($10^6 M_\odot$) and low-density ($\rho = 10^{-24}\,\mathrm{g/cm^3}$) model. The density profile of FG stars is also included for reference, represented by a black dashed line. *Right column*: mass distribution of Y in SG stars. These distributions are obtained by summing the masses of stars within each Y bin, and then normalizing each distribution to its maximum value. The black dashed vertical lines denote the pristine gas composition while the solid black line represents the normalized cumulative mass as a function of Y. In each panel we also report the Y spread (σ), computed as the standard deviation of the distribution. The evolutionary times are indicated on the left of each set of panels. From top to bottom: t = 17, 34, 46, 55 Myr.

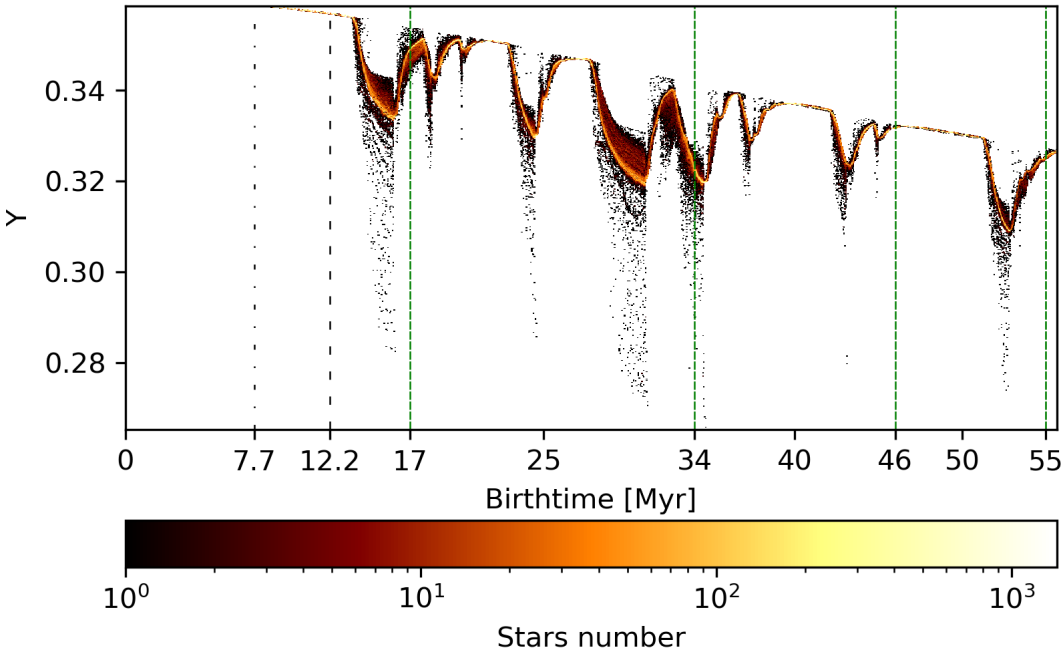

Figure 4.9. Helium mass fraction (Y) and stars birthtime 1024x1024 colormap for the M6-Infall24 model. The color scale indicates the number of SG stars. The green dashed vertical lines represent the reported evolutionary times (17, 34, 46, 55 Myr). The black vertical lines mark the time at which the infalling gas (dashed line) crosses the center of the cluster and the onset of the injection of AGB ejecta (dash dotted line). In this scenario $t_{\rm inf} = 12.2\,$Myr and $t_{\rm AGB} = 7.7\,$Myr (see Table 3.2).

4.2.2.2 Iron-to-hydrogen abundance ratio [Fe/H]

In Figure 4.10, we present the same configuration as shown in Figure 4.8, but this time in terms of the iron-to-hydrogen abundance ratio [Fe/H] rather than the helium mass fraction Y.

The mass distribution of [Fe/H] will vary based on Type Ia SN, AGB ejecta and dilution from infalling pristine gas. Additionally, in this model, the more pronounced contribution of SNeIa explosions in enriching the gas with iron will become evident. In this scenario, the cluster's higher mass enables the retention of more iron within its gravitational well, enhancing star formation with higher iron-to-hydrogen abundance.

At 17 Myr, the density of SG stars peaks in the central regions ($\rho_\star$=10^{-17}g/cm^3), surpassing that of FG stars within r<0.2 pc. In this zone, the prevailing stellar group is metal-poor ([Fe/H]<-1.5), supported by a smaller population with higher metallicity (-1.5<[Fe/H]<-1.3), and a negligible presence of stars at -1.3<[Fe/H]<-1.1. The density profile suggests that the metal-poor population dominates the system up to distances beyond 10 pc, constituting 90% of the system's mass. The remaining 10% is predominantly composed of stars with higher metallicity.

At 34 Myr, the density of SG stars reaches its peak at the center, around $\rho_\star \simeq 10^{-16}$g/cm^3, composed of the most metal-poor and more [Fe/H]-enhanced populations. Examining the density profile further shows a notable stellar population with -1.3<[Fe/H]<-1.1 within r<2pc, contributing a few percent to the total mass, and an almost negligible formation of SG stars at -1.1<[Fe/H]<-0.9. Additionally, the contribution of stars at -1.5<[Fe/H]<-1.3 has grown representing, at this time, approximately 30% of the total mass, as indicated in the right-hand graph.

At the subsequent time step (t = 46 Myr), continuous star formation persists for populations with [Fe/H]>-1.5, contributing to approximately 40% of the total mass.

No significant difference is visible in the plots at the final step, 55 Myr.

The formed SG population dominates the system within r<0.2 pc, beyond which the first-generation population takes over. The nearly two orders of magnitude higher central densities of this model confirm that the mass of the system plays a fundamental role in SG star formation, even in the presence of type Ia SNe. In comparison with the SNeIa-free case studied by Yaghoobi et al. (2022), a similar density peak is reached ($\rho \approx 10^{-16}\,\mathrm{g/\,cm^3}$), but in a more confined region, with star formation extending to the outer regions of the box. Furthermore, the stellar population is generally more He-rich, featuring a structured mass distribution function with peaks and less uniformity. Finally, the total mass of this model after 55 Myr is $3.0 \times 10^4\,\mathrm{M_\odot}$, half the mass of the corresponding model without SNeIa after 71 Myr.

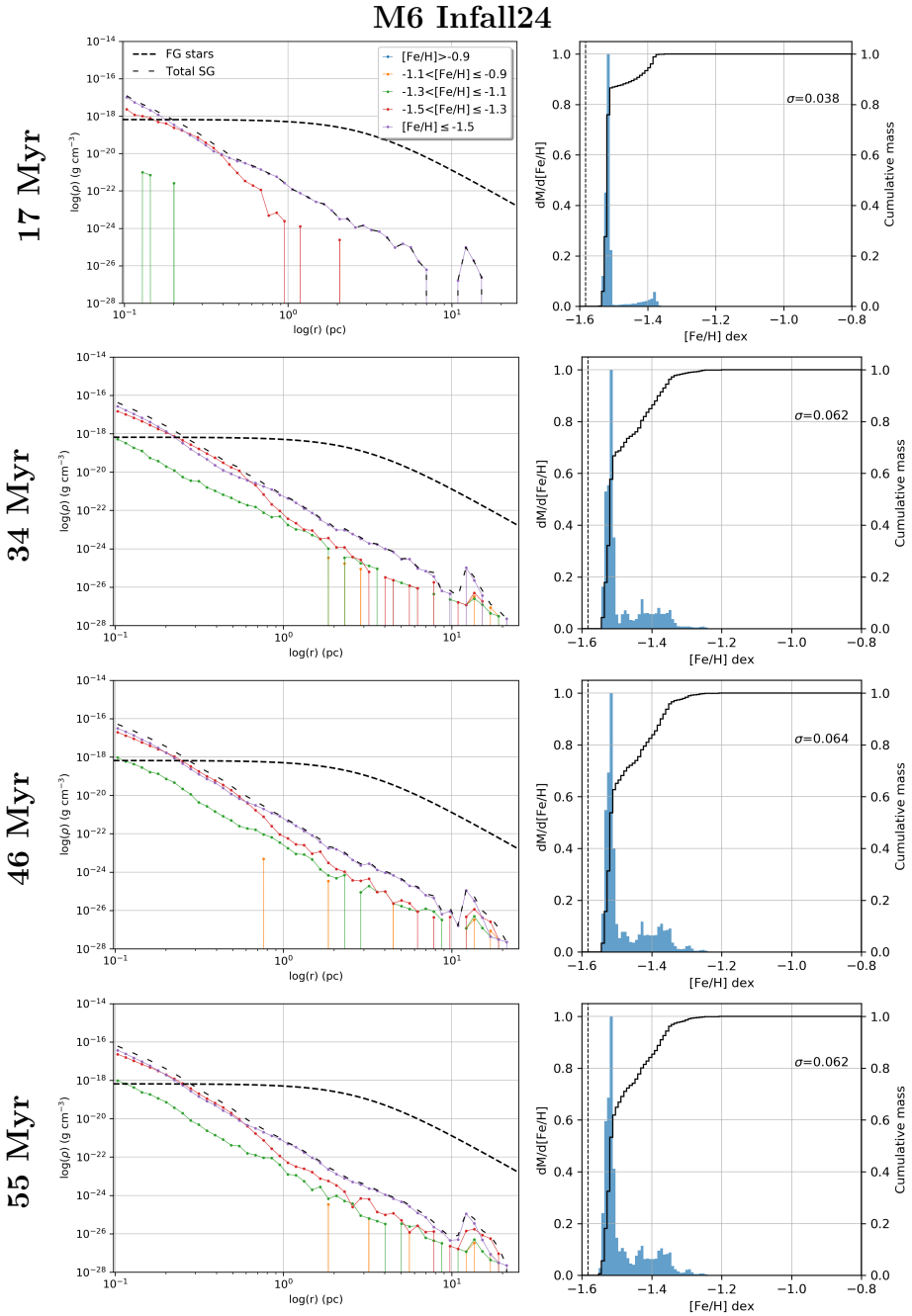

Figure 4.10. *Left column*: total density profile of SG stars and density profiles of SG stars categorized by [Fe/H] ratio (Y) bins for the high-mass ($10^6 M_\odot$) and low-density ($\rho = 10^{-24}$ g/ cm^3) model. The density profile of FG stars is also included for reference, represented by a black dashed line. *Right column*: mass distribution of [Fe/H] in SG stars. These distributions are obtained by summing the masses of stars within each [Fe/H] bin, and then normalizing each distribution to its maximum value. The black dashed vertical lines denote the pristine gas composition while the solid black line represents the normalized cumulative mass as a function of [Fe/H]. In each panel we also report the [Fe/H] spread (σ), computed as the standard deviation of the distribution. The evolutionary times are indicated on the left of each set of panels. From top to bottom: t = 17, 34, 46, 55 Myr.

4.3 Model M6-Infall23

In this section we present our last model, a cluster characterized by a FG with a mass of $10^6\,M_\odot$ and with a pristine gas density ten times higher than previous models ($\rho_{\rm pg} = 10^{-23}\,{\rm g/\,cm^3}$). With respect to the less massive FG , the start of pristine gas infall is anticipated in this case. By applying equations (1) and (2), we determine that the infall starts at $t_{\rm inf} = 3$ Myr and the onset of AGB ejecta is at $t_{\rm AGB} = 7.7$ Myr.

A higher interstellar medium (ISM) density, compared to the conditions explored in the previous sub-sections, is anticipated to significantly influence the cluster's ability to accumulate mass (Naiman et al. 2011) and give rise to SG stars.

4.3.1 Dynamical evolution of the gas and SG stars spatial distribution

In the next two figures, we present density, pressure normalized to the Boltzmann constant, and temperature maps (Figure 4.11), along with the spatial distribution of SG stars (Figure 4.12) from our simulation, which includes denser infalling gas in the x-y plane computed at 17, 34, 46, and 50 Myr.

At the initial timestep (t = 17 Myr), a substantial volume within the box is occupied by infalling pristine gas, entering from the left side and moving towards the end. On the right side, a notable accumulation of gas (ρ=$10^{-22}\,{\rm g/\,cm^3}$) with low pressure (P/k_b=$10^4\,{\rm K/\,cm^3}$) and temperature ($\sim 10^3 K$) is observed, forming an accretion tail directed towards the central regions. This structure appears to be fed by the warmer and less dense gas above and below it. In the central regions, there is a compact concentration (ρ>$10^{-21}\,{\rm g/\,cm^3}$) of gas that has completely cooled (T=T_{floor}), distributed on an elongated shape along the x-axis. Lastly, a circular region is discernible. This region possesses a radius of a few parsecs, exhibiting a density comparable to pristine gas but with higher temperature and pressure (T>T_{pg}; P/k_b>P_{pg}/k_b). The surface density maps of stellar mass reveal significant star formation at the initial evolutionary times, with stars forming throughout the computational volume and a density peak at the very center ($\Sigma_\star > 10^4\,M_\odot/\,{\rm pc^2}$). Additionally, an elongated structure is observed along the x-axis, corresponding to the direction of motion of infalling gas. As mentioned earlier, this extended structure is attributed to the higher ram pressure of pristine gas compared to the low-density cases studied previously.

At 34 Myr, similar to the previous models, we observe recent activity from a SN Ia. In this case, in particular, the supernova bubble can be observed with a thin shell at high densities and pressures ($\rho > 10^{-22}\,{\rm g/\,cm^3}$; $P/k_b > 10^6\,{\rm K/\,cm^3}$) and high temperature (T$\simeq 10^7 K$). The shell surrounds is a nearly homogeneous cavity

at lower density, with elevated values of temperature and pressure. In the central zones, as in the previous timestep, there is a high-pressure and cool gas filament, supplied by an elongated accretion tail along the x-axis, but narrower compared to the earlier phase. The stellar mass surface density map in Figure 4.12 reveals ongoing star formation even outside the cluster centre, where a diffuse stellar component is present at density $\Sigma \approx 10^2\,\mathrm{M}_\odot/\,\mathrm{pc}^2$.

At the following time (t = 46 Myr), the system seems to be regaining mass after undergoing a "clearing" phase, especially in the outer regions affected by supernova explosions. In this instance, the right side of the box displays lower density and pressure, accompanied by temperatures around $\sim 10^5\,\mathrm{K}$. Meanwhile, the left side consists of infalling pristine gas. As observed in previous timesteps, the central region of the box exhibits the highest density, fully cooled, but at this time, it appears more compact with a circular shape and a "stripped" and less dense tail on the right side of the box. Numerous instabilities are present on the left of the centre, reminescent of the interaction of the disrupted shell with the infalling gas. Furthermore, as shown in Figure 4.12, the stellar component appears to have spatially consolidated without significant differences compared to the previous time.

At the last timestep, 50 Myr, the system shows minimal changes. The inward progression of infalling gas is more pronounced in the central regions. Simultaneously, the additional energy from SNeIa explosions seems to have eradicated the accretion tail structure, leading to further heating at the center. This is associated with a slowdown in SG star formation. The surface density map of stellar mass remains nearly identical to the previous one.

In summary, throughout the entire simulation period, the gas has exhibited a distinct evolution compared to low-density scenarios. The increased density of the interstellar medium contributes to increased ram pressure, accompanied to an extended star formation in the outer regions. Besides the more abundant pristine gas, also the more massive stellar FG plays a crucial role in facilitating significant star formation.

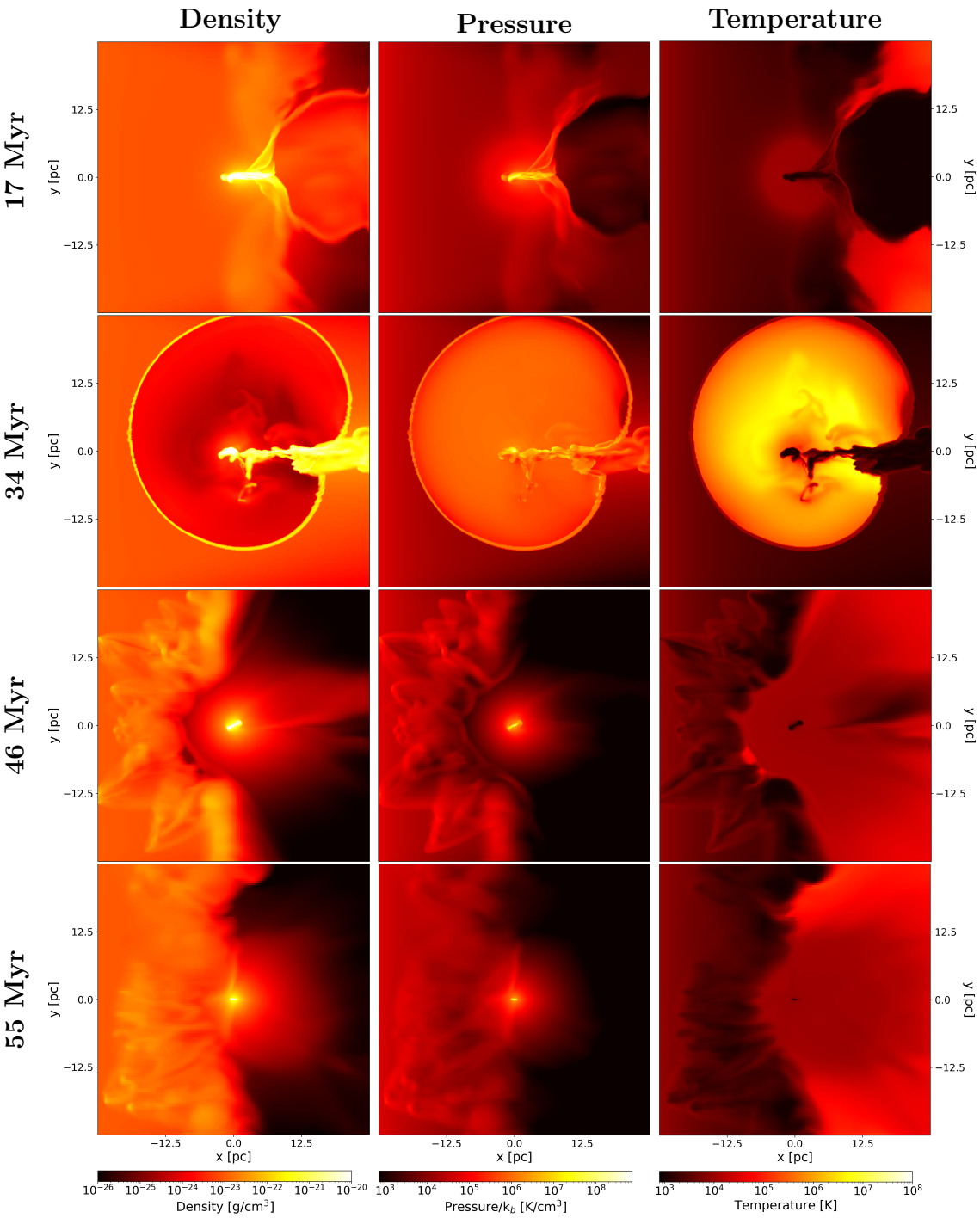

Figure 4.11. Two-dimensional slice maps of the gas density (*left-hand panels*), pressure (*middle panels*) and temperature (*right-hand panels*) in the x-y plane are presented at various stages of evolution for the M6-Infall23 model, a high mass ($10^6 M_\odot$) and high density ($\rho = 10^{-23}\,\mathrm{g/cm^3}$) simulation. The infall gas, as implemented, enters from the left side of the computational box. The evolutionary times are indicated on the left of each set of panels. From top to bottom: $t =$ 17, 34, 46, 50 Myr.

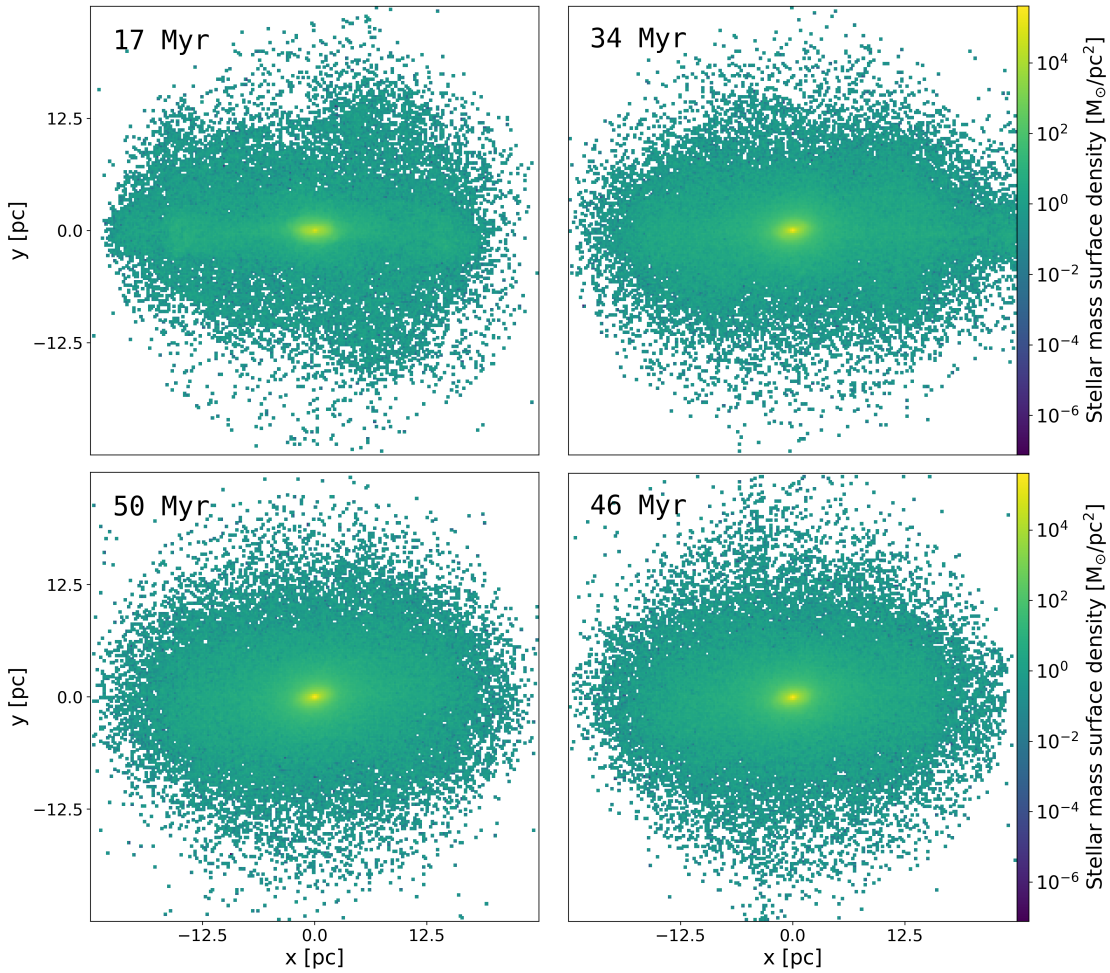

Figure 4.12. Two-dimensional projection maps of the surface stellar density in the x-y plane are presented at various stages of evolution for the M6-Infall23 model, a high mass ($10^6 M_\odot$) and high density ($\rho = 10^{-23}\,\mathrm{g/cm^3}$) simulation. Clockwise, from top to bottom: t = 17, 34, 46, 50 Myr.

4.3.2 Stellar abundances

4.3.2.1 Helium mass fraction Y

In Figure 4.13, we plot the density profiles of SG, both total and for various helium composition, together with the Y mass distributions for the high-mass high-density model (M6-Infall23), at different evolutionary times. In Figure 4.14, we additionally present a colormap representing the number of SG stars in the Y-birthime plane.

In contrast to the previous models, the results at 17 Myr reveal a diverse range of helium abundances within SG stars. In the central regions and within r<0.4 pc,

the total stellar density is dominated by He-intermediate stars ($0.27 < Y < 0.30$). This population is the dominant SG one up to ∼1.1pc, beyond which the most He-poor stars ($Y < 0.27$) dominate, presenting a flatter distribution and extending up to 20 pc. Predominantly formed in the central regions, He-rich populations ($Y > 0.30$) account for less than 10% of the system's mass, as depicted in the right panel. A notable feature in the distribution plot is the peak at Y_{pg}, representing a few percentiles of the cluster's mass. This specific fraction of stars underwent star formation on infalling gas without AGB ejecta contamination, evident in its density profile stretching across the entire box and dominating at large distances from the centre. This characteristic is also highlighted in the map in Figure 4.14, showing a significant number of stars formed at this Y value in various stages of star formation.

At the subsequent timestep (t = 34 Myr), compared to the previous period, there is a concentration of He-rich stars ($Y > 0.33$) at innermost radii, becoming denser than FG stars at approximately 0.1 pc. The increase in stellar mass at $Y > 0.30$ is evident also from the mass distribution plot on the right. Additionally, the plot on the right reveals another prominent peak around $Y \simeq 0.275$. Recalling that at this timestep, gas maps (Figure 4.11) showed a SNeIa bubble, it is noteworthy that in the following period, star formation proceeds, leading to a rapid increase in Y. As analyzed in the previous model, this behaviour can be attributed to a formation of SG out of undiluted AGB ejecta due to the prevented accretion of infalling gas caused by the SN explosion.

At 46 Myr, after a previous formation in the central regions, the population of He-poor stars has significantly grown in mass, exceeding the density of FG stars at a radius smaller than 0.1 pc, similar to He-rich stars. The increase of this population is also evident in the Y-mass distribution plot, showing a minor peak at $Y<0.27$. Additionally, this plot indicates a rise in the He-rich population, as seen in a peak creating a discontinuity in the cumulative mass distribution graph at $0.325<Y<0.35$. The formation of this sub-population is evident in Figure 4.14 at ∼40 Myr. The reason for this formation is attributed to a significant type Ia SN activity that interrupted the dilution from infalling gas for a prolonged period.

At the final timestep, 50 Myr, the system appears stable, showing no major changes in density or mass distribution concerning the Y content.

In conclusion, differently from the previous model (M6-Infall24), the dominant population in the second generation of stars is the He-intermediate group ($0.27<Y<0.30$). We observe a particularly efficient dilution of AGB ejecta with infalling gas. The injection of energy and mass from SNeIa affects the evolution of the stellar population, manifesting in more compactness in central regions with higher density peak and a broader distribution in outer regions compared to scenarios without SNeIa (see Yaghoobi et al. 2022).

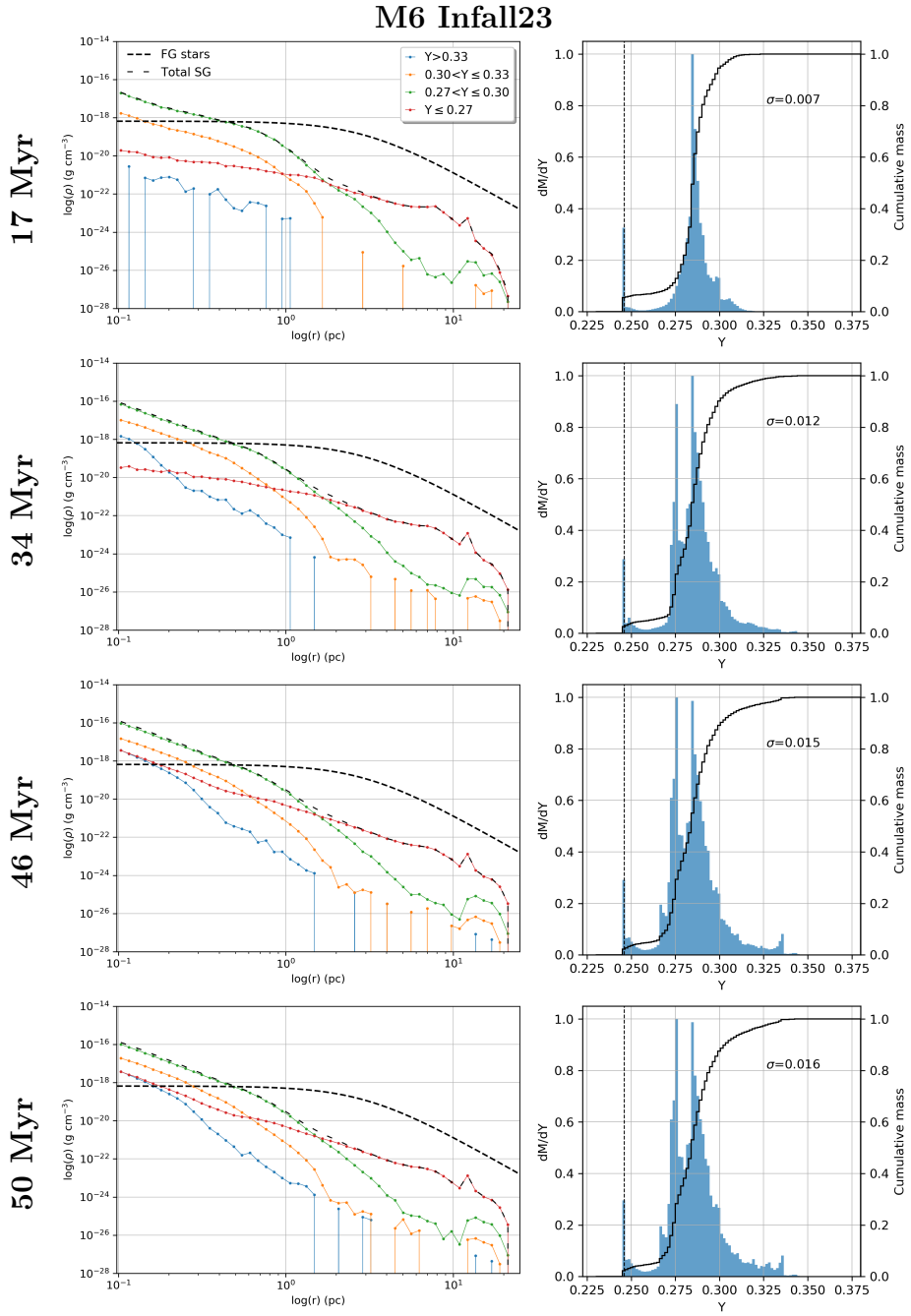

Figure 4.13. *Left column*: total density profile of SG stars and density profiles of SG stars categorized by helium mass fraction (Y) bins for the high-mass ($10^6 M_\odot$) and high-density ($\rho = 10^{-23}\,\mathrm{g/\,cm^3}$) model. The density profile of FG stars is also included for reference, represented by a black dashed line. *Right column*: mass distribution of Y in SG stars. These distributions are obtained by summing the masses of stars within each Y bin, and then normalizing each distribution to its maximum value. The black dashed vertical lines denote the pristine gas composition while the solid black line represents the normalized cumulative mass as a function of Y. In each panel we also report the Y spread (σ), computed as the standard deviation of the distribution. The evolutionary times are indicated on the left of each set of panels. From top to bottom: t = 17, 34, 46, 50 Myr.

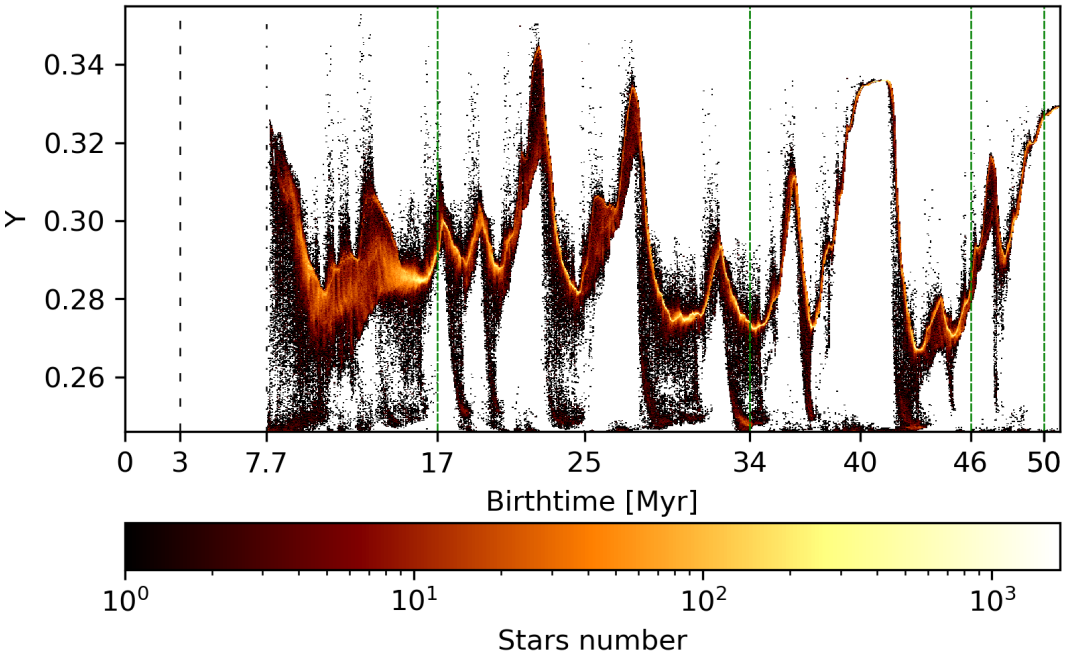

Figure 4.14. Helium mass fraction (Y) and stars birthtime 1024x1024 colormap for the M6-Infall23 model. The color scale indicates the number of SG stars. The green dashed vertical lines represent the reported evolutionary times (17, 34, 46, 50 Myr). The black vertical lines mark the time at which the infalling gas (dashed line) crosses the center of the cluster and the onset of the injection of AGB ejecta (dash dotted line). In this scenario $t_{\rm inf} = 3\,$Myr and $t_{\rm AGB} = 7.7\,$Myr (see Table Table 3.2).

4.3.2.2 Iron-to-hydrogen abundance ratio [Fe/H]

In Figure 4.15, we present the same configuration as shown in Figure 4.13, but this time in terms of the iron-to-hydrogen abundance ratio [Fe/H] rather than the helium mass fraction Y.

At 17 Myr, populations with -1.5<[Fe/H]<-1.3 dominate the innermost regions of the system (r < 1 pc), surpassing the density of FG stars at r < 0.3 pc reaching a peak at $\rho_\star = 10^{-16}\,$g/ cm^3. The outermost regions, on the other hand, are dominated by the most metal-poor stars ([Fe/H]<-1.5). A third population with -1.3 < [Fe/H] <-1.1 has formed in the central zone of the system, negligible in mass as seen in the right-hand graph. There is also a very small and negligible presence of a more metal-rich population (-1.1<[Fe/H]<-0.9). The mass distribution of [Fe/H], similar to previous models, exhibits a multi-peaked distribution, that extends for nearly 0.2 dex at the right of the pristing gas value .

At 34 Myr, there is an increased formation of [Fe/H]-intermediate stars (-1.3<[Fe/H]<-1.1), distributed throughout the system up to radii of 20 pc. There is also a small formation of stars with -1.1<[Fe/H]<-0.9 at radii less than 1 pc. Looking at the mass distribution of [Fe/H], it becomes evident that metal-poor

stars have a strong dominance.

At the next timestep (46 Myr), we observe no significant alterations in the iron abundance of stellar populations, evident in both the density profile and the mass distribution of [Fe/H].

Finally, 4 Myr after, there are no substantial changes in the system, with an almost unaltered density profile and a mass distribution of [Fe/H].

The SG population dominates the central region of the system within r$<$0.4 pc while beyond the FG becomes more prominent. This pattern is similar to the M6-Infall24 model, but with the higher-density scenario displaying nearly three orders of magnitude higher density at r=10 pc. In comparison to the SNeIa-free case studied by Yaghoobi et al. (2022), a similar density peak is reached, but in a more confined region, with star formation extending to the outer regions of the box. Additionally, the stellar population in this model tends to be more He-rich, featuring a more structured mass distribution function with various peaks and less uniform. Finally, the total mass of this model after 50 Myr is $6.7 \times 10^4\,M_\odot$, representing approximately a $\sim$66% reduction in mass compared to the scenario without SNeIa after 71 Myr.

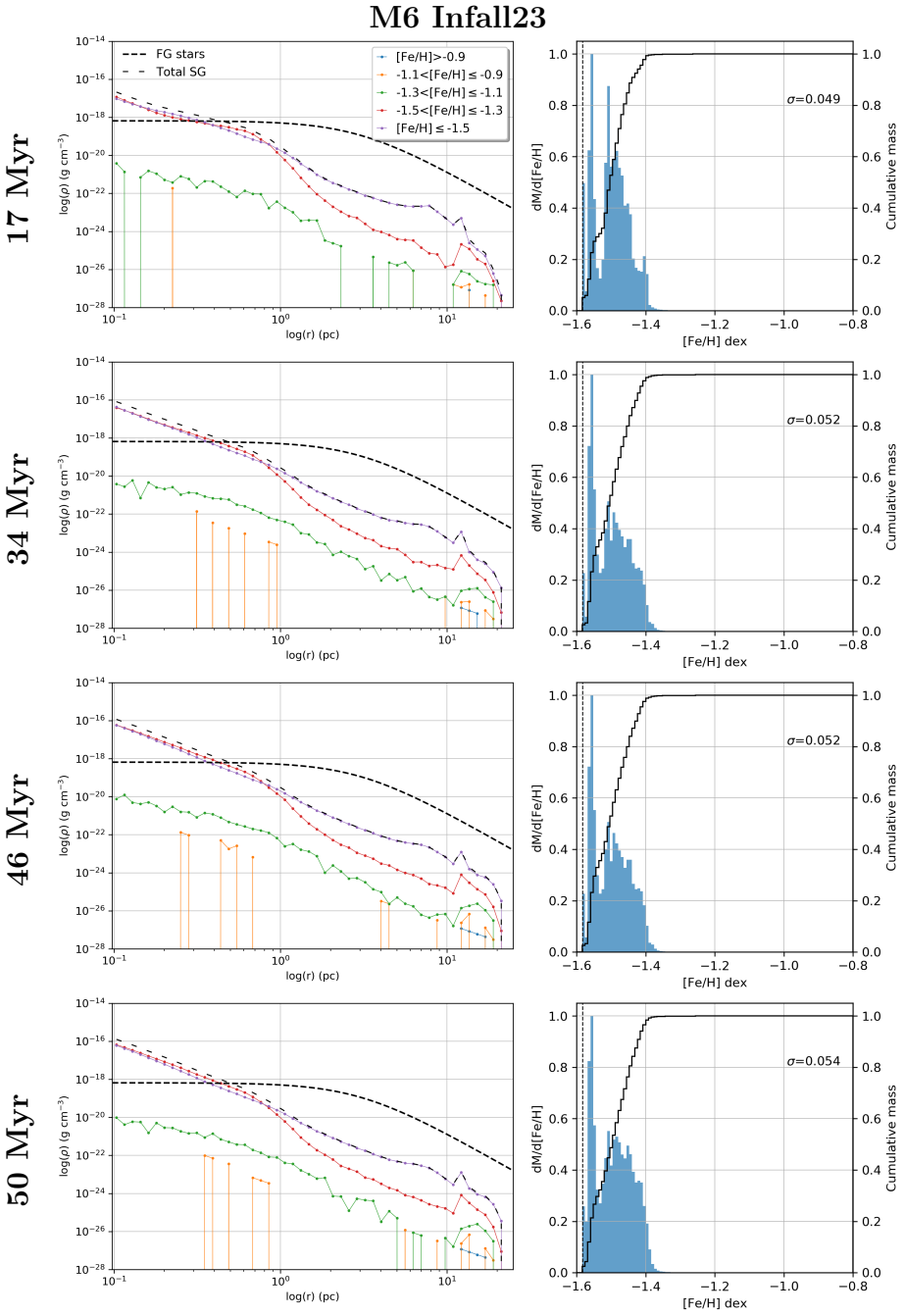

Figure 4.15. *Left column*: total density profile of SG stars and density profiles of SG stars categorized by [Fe/H] ratio bins for the high-mass ($10^6 M_\odot$) and high-density ($\rho = 10^{-23}\,\mathrm{g/cm^3}$) model. The density profile of FG stars is also included for reference, represented by a black dashed line. *Right column*: mass distribution of [Fe/H] in SG stars. These distributions are obtained by summing the masses of stars within each [Fe/H] bin, and then normalizing each distribution to its maximum value. The black dashed vertical lines denote the pristine gas composition while the solid black line represents the normalized cumulative mass as a function of [Fe/H]. In each panel we also report the [Fe/H] spread (σ), computed as the standard deviation of the distribution. The evolutionary times are indicated on the left of each set of panels. From top to bottom: t = 17, 34, 46, 50 Myr.

4.4 Second generation star formation

In this section we show the evolution of the SFR and of the cumulative mass of our simulated clusters and compare our results with the ones of Yaghoobi et al. (2022).

Focusing on the SFH, in the top panel of Figure 4.16, in the $10^5\,M_\odot$ model, star formation begins after a delay compared to the start of AGB mass return and the infall gas crossing the cluster center. On the other hand, star formation in the $10^6\,M_\odot$ models starts either in correspondence with the arrival of accreted gas at the center (in the high-density model M6-Infall23) or the beginning of AGB mass return (in the low-density model M6-Infall24). This can be attributed to the deeper gravitational potential and larger amount of ejected AGB gas of these clusters (for the injection times of AGB material and pristine gas, refer to Table 3.2). The plot also shows the weak star formation for the M5-Infall24 case, with three hiatus periods, one of which is particularly extended at around 40 Myr, as mentioned in subsection 4.1.2. In contrast, the high-mass models show continuous star formation throughout the entire simulation, with the high-density case exhibiting the highest average SFR, in agreement with the results of in Calura et al. (2019), Lacchin et al. (2021), and Yaghoobi et al. (2022).

The cumulative SG mass growth of the three models follows different trends. The high-mass model is characterised by a steep rise at early times and a flatter behaviour at late times. On the other hand, the low-mass model shows a more gradual growth, with a flatter slope at early times.

Comparing with the results for the same models, but without SNe Ia explosions, the M5-Infall24 model is significantly influenced by SNeIa feedback, leading to a substantial limitation of pristine gas reaccretion. The supernovae affect the SG star formation at later times ($t \gtrsim 30$ Myr), limiting the total mass of the SG population. In a case with a shallow potential well like the one of the low-mass model, we note extended hiatus periods in star formation. The high-mass models (M6-Infall24; M6-Infall23) show less differences with the homologous models without SNe, with an almost constant SFR throughout the evolutionary time, although with greater dispersion and a slightly lower average value. Regarding the mass, as discussed earlier, the three models formed SG stars with masses of $1.1{\cdot}10^3\,M_\odot$ for the case M5-Infall24, $3.0{\cdot}10^4\,M_\odot$ for the case M6-Infall24, and $6.7{\cdot}10^4\,M_\odot$ for the case M6-Infall23. This indicates a reduction in mass ranging from 50% to 66% for the high-density scenario compared to the results of Yaghoobi et al. (2022). It's worth noting that this evaluation was conducted at different evolutionary times (50-55 Myr in this study and 71 Myr in Yaghoobi et al. 2022).

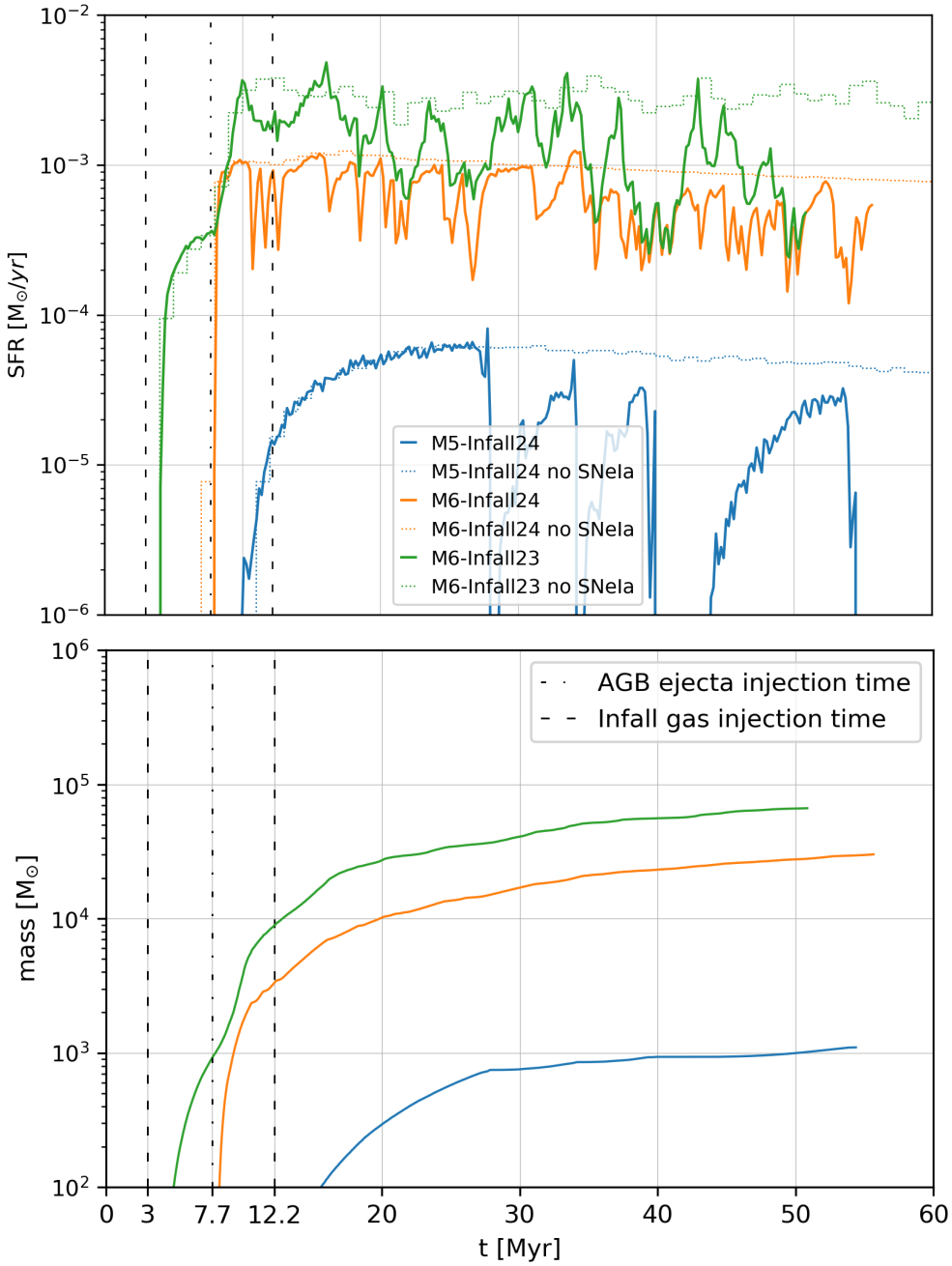

Figure 4.16. *Top panel*: SG star formation rates vs. time for our simulated clusters (solid lines) and for the same models without SNe Ia explosions (dotted lines). *Bottom panel*: Cumulative SG stellar mass formed in our simulated clusters. The black vertical lines mark the time at which the infalling gas (dashed lines) crosses the center of the cluster in each model and the onset of the injection of AGB ejecta (dash dotted line). Specifically, the models M5-Infall24 and M6-Infall23 both have $t_{\rm inf}$= 3 Myr while the M6-Infall24 model has $t_{\rm inf}$= 12.2 Myr.All three models share the same asymptotic giant branch timescale $t_{\rm AGB}$= 7.7 Myr (see Table 3.2).

Chapter 5

Conclusions

By means of hydrodynamic simulations, this thesis explores the formation of a second generation of stars in three clusters moving within a uniform gas distribution, influenced by first generation Type Ia SN explosions from the first generation. The main goal is to understand how SNeIa feedback impacts the duration of the SG star formation epoch and the chemical properties of the SG population.

The three simulations depict FG clusters with different masses ($10^{5-6}\,M_\odot$) and ambient gas densities ($\rho_{pg} = 10^{23-24}\,g/\,cm^3$), representing the interaction of young clusters with fresh gas from a dwarf galaxy disk. Specifically, the models include low mass ($10^5\,M_\odot$) and low density ($10^{24}\,g/\,cm^3$) denoted as M5-Infall24, high mass ($10^6\,M_\odot$) and low density as M6-Infall24, and high mass and high density ($10^{23}\,g/\,cm^3$) as M6-Infall23. The adopted models are meant to extend the work of Lacchin et al. (2021), which shares the same setup but with an FG mass of $10^7\,M_\odot$ while the ISM density values represent typical values observed in star-forming galaxies.

The simulations begin at the end of the FG Type II SN epoch, when the ejecta of the most massive AGB stars are released in the cluster and the SG star formation begins. The models are simulated through a wind tunnel experiment, involving an infall of homogeneous pristine gas with the same composition as FG stars, entering from one side of the box at a constant velocity. In addition to star formation, mass and energy return from FG AGB stars, along with radiative cooling, are implemented.

An fundamental aspect in the study of multiple populations in GCs is the chemistry of these populations. In this thesis, we examine the chemical properties of the SG by analyzing the helium mass fraction (Y) and the iron-to-hydrogen abundance ([Fe/H]). Our analysis aims to explore the dependence of SG chemistry on the cluster's mass and its surrounding environment.

We can summarize our analysis as follows:

(i) In all scenarios, the central part of the box has dense and cold gas – ideal conditions for star formation, which primarily occurs in these regions. As time progresses, the amount of cold gas decreases in all models due to the increasing rate of SNeIa (Figure 3.3 and 3.4). The lower-mass model, M5-Infall24, is the most affected, struggling to counteract the energy injection from SNeIa, resulting in less gas fall into the central, star-forming regions. In the higher-mass cases, the deeper potential allows for significant concentration of cold gas at the center and, at times, the formation of an accretion tail. However, with more SNeIa, the M6-Infall24 generally exhibits a warmer and less dense environment. This is not observed in the high-density case (M6-Infall23), where cold and dense gas is present throughout the box from the first timestep. Although star formation is distributed across space, stars are more diffuse in the outskirts compared to the less dense model counterpart. This phenomenon is favored by the higher ram pressure resulting from the increased gas density.

(ii) In all models, the SG dominates at the very center of the cluster, exhibiting a multi-peaked density distributions for various chemical compositions. In low-density models, He-rich populations (Y $>$ 0.33) prevail, with a particularly uniform mass distribution of Y and low spread in the case of low mass (M5-Infall24), and a more discrete and spread-out distribution in the case of high mass (M6-Infall24). In the case of M6-Infall23, we observe flatter distributions compared to the previous ones, with He-intermediate stars dominating ($0.27 < Y < 0.30$). This is because the high density of pristine gas in this scenario facilitates the dilution between AGB material and infalling gas.

Comparing with the case without SNeIa (Yaghoobi et al. 2022), it becomes evident that feedback significantly alters the chemistry of the low density clusters. The case without SNe predicts a homogeneous distribution based on initial star formation predominantly composed of AGB material, diluted over time by infalling gas with lower helium concentration. Introducing SN Ia feedback, the energy injection sweeps away gas from star-forming regions, slowing down SF and hindering material dilution. It is interesting to note that in the M5-Infall24 model, there are hiatuses in star formation, one of which is particularly prolonged, allowing the creation of a bimodal structure in Y at later times. The M6-Infall23 model, despite exhibiting a peaked He distribution attributed to SNe, shows a mean value in Y ($\overline{Y} \approx 0.286$) comparable to the scenario without SNe.

(iii) Regarding the iron abundances in SG, compared to the helium distributions, we observe more uniform and single-peak distributions. The more metal-poor populations dominate the central regions in all models. In the case with

lower mass and density (M5-Infall24), the SG is almost entirely composed of stars with [Fe/H] <-1.5, attributed solely to AGB material and the inefficient ability to retain material from SNeIa due to the low gravitational potential. The higher mass cases show populations with a higher Fe content, with a range in [Fe/H] of approximately 0.2 dex, confirming that the deeper potential allows for the retention of SNeIa feedback. The lower-density model exhibits a more peaked distribution at low metallicity values, while at higher density, the [Fe/H]-intermediate populations (-1.5<[Fe/H]<-1.3) correspond to about half of the population. This trend, similar to what was found for Y, is due to the ability of the M6-Infall23 model to undergo star formation outside the central regions, supported by flatter density profiles, coupled with the continuous sweeping away of gas by SNeIa.

(iv) The SFH of the three models is closely dependent on the cluster's mass, showing more than an order of magnitude difference in final SG mass in the case of M5-Infall24 compared to the other two scenarios, with three hiatuses during the simulation. The higher-mass models exhibit continuous SF throughout the integration time, with a higher SFR in the M6-Infall23 model. Compared to the case without SNe, the models show a lower SFR at all times Additionally, in the case without SNe, the M5-Infall24 model does not show hiatuses in star formation. This lower SFR in the three models results in a reduced mass of the SG. The SG mass values for the three models after 50 Myr are $1.1 \cdot 10^3\,M_\odot$ for the M5-Infall24 case, $3.0 \cdot 10^4\,M_\odot$ for the M6-Infall24 case, and $6.7 \cdot 10^4\,M_\odot$ for the M6-Infall23 case, indicating a reduction in mass ranging from 50% to 66% compared to the results in Yaghoobi et al. (2022).

It is worth noting that the multi-peaked mass distributions of Y and [Fe/H], attributed to SNeIa feedback, might be associated with the characteristic discreteness observed in multiple populations within globular clusters.

The analyzed simulations highlight that Type Ia supernova feedback significantly alters the evolution of globular clusters, markedly reducing star formation and giving rise to populations with distinctive chemical features. This aspect could be a key element in understanding the formation of globular clusters, requiring further analysis and investigation.

Finally, our models need also to be improved with the inclusion of relevant physical mechanisms which are expected to affect mass accretion and star formation, such as ionizing feedback from SG stars which could lead to a further decrease of the SFR and a non-static FG distribution composed of "live particles". Furthermore, expanding the analysis to include a greater number of chemical elements, such as sodium and oxygen, will contribute to a more comprehensive understanding of chemical properties of multiple populations.

Bibliography

Aarseth S. J., 1963, MNRAS, 126, 223

Barnes J., Hut P., 1986, Nature, 324, 446

Bastian N., Lardo C., 2015, MNRAS, 453, 357

Bastian N., Lardo C., 2018, ARA&A, 56, 83

Bastian N., Lamers H. J. G. L. M., de Mink S. E., Longmore S. N., Goodwin S. P., Gieles M., 2013a, MNRAS, 436, 2398

Bastian N., Cabrera-Ziri I., Davies B., Larsen S. S., 2013b, MNRAS, 436, 2852

Bondi H., 1952, MNRAS, 112, 195

Breen P. G., 2018, MNRAS, 481, L110

Bryan G. L., et al., 2014, ApJS, 211, 19

Calura F., Few C. G., Romano D., D'Ercole A., 2015, ApJ, 814, L14

Calura F., D'Ercole A., Vesperini E., Vanzella E., Sollima A., 2019, MNRAS, 489, 3269

Calura F., et al., 2022, MNRAS, 516, 5914

Carretta E., et al., 2009, A&A, 505, 117

Charbonnel C., Chantereau W., Krause M., Primas F., Wang Y., 2014, A&A, 569, L6

Ciotti L., D'Ercole A., Pellegrini S., Renzini A., 1991, ApJ, 376, 380

Colella P., 1990, Journal of Computational Physics, 87, 171

Cottrell P. L., Da Costa G. S., 1981, ApJ, 245, L79

Couchman H. M. P., 1991, ApJ, 368, L23

D'Ercole A., Vesperini E., D'Antona F., McMillan S. L. W., Recchi S., 2008, MNRAS, 391, 825

D'Ercole A., D'Antona F., Vesperini E., 2011, MNRAS, 415, 1304

D'Ercole A., D'Antona F., Vesperini E., 2016, MNRAS, 461, 4088

Dalessandro E., Lapenna E., Mucciarelli A., Origlia L., Ferraro F. R., Lanzoni B., 2016, ApJ, 829, 77

Dalessandro E., et al., 2019, ApJ, 884, L24

Decressin T., Meynet G., Charbonnel C., Prantzos N., Ekström S., 2007a, A&A, 464, 1029

Decressin T., Charbonnel C., Meynet G., 2007b, A&A, 475, 859

Dehnen W., 2001, MNRAS, 324, 273

Dejonghe H., 1987, MNRAS, 224, 13

Denissenkov P. A., Hartwick F. D. A., 2014, MNRAS, 437, L21

Elmegreen B. G., 2017, ApJ, 836, 80

Fryxell B., et al., 2000, ApJS, 131, 273

Gieles M., et al., 2018, MNRAS, 478, 2461

Gratton, R. G. et al., 2013, A&A, 549, A41

Gratton R., Sneden C., Carretta E., 2004, ARA&A, 42, 385

Gratton R., Bragaglia A., Carretta E., D'Orazi V., Lucatello S., Sollima A., 2019, A&A Rev., 27, 8

Greggio L., 2005, A&A, 441, 1055

Hockney R. W., Eastwood J. W., 1981, Computer Simulation Using Particles

Hopkins P. F., Murray N., Quataert E., Thompson T. A., 2010, MNRAS, 401, L19

Jessop C., Duncan M., Chau W. Y., 1994, Journal of Computational Physics, 115, 339

Khokhlov A., 1998, Journal of Computational Physics, 143, 519

Krause M., Charbonnel C., Decressin T., Meynet G., Prantzos N., 2013, A&A, 552, A121

Kravtsov A. V., Klypin A. A., Khokhlov A. M., 1997, ApJS, 111, 73

Kroupa P., 2001, MNRAS, 322, 231

Lacchin E., Matteucci F., Vincenzo F., Palla M., 2020, MNRAS, 495, 3276

Lacchin E., Calura F., Vesperini E., 2021, MNRAS, 506, 5951

Lada C. J., Lada E. A., 2003, ARA&A, 41, 57

Lardo C., Bellazzini M., Pancino E., Carretta E., Bragaglia A., Dalessandro E., 2011, A&A, 525, A114

Lützgendorf N., et al., 2013, A&A, 552, A49

Marino A. F., et al., 2014, MNRAS, 437, 1609

Menon H., Wesolowski L., Zheng G., Jetley P., Kale L., Quinn T., Governato F., 2015, Computational Astrophysics and Cosmology, 2, 1

Mignone A., Bodo G., Massaglia S., Matsakos T., Tesileanu O., Zanni C., Ferrari A., 2007, ApJS, 170, 228

Milone A. P., et al., 2015, ApJ, 808, 51

Minniti D., Geisler D., Peterson R. C., Claria J. J., 1993, ApJ, 413, 548

Naiman J. P., Ramirez-Ruiz E., Lin D. N. C., 2011, ApJ, 735, 25

Plummer H. C., 1911, MNRAS, 71, 460

Prantzos, N. Charbonnel, C. 2006, A&A, 458, 135

Press W. H., Teukolsky S. A., Vetterling W. T., Flannery B. P., 1992, Numerical recipes in FORTRAN. The art of scientific computing

Price D. J., et al., 2018, PASA, 35, e031

Rasera Y., Teyssier R., 2006, A&A, 445, 1

Renzini A., Buzzoni A., 1986, in Chiosi C., Renzini A., eds, Spectral Evolution of Galaxies. Springer Netherlands, Dordrecht, pp 195–235

Revaz Y., Jablonka P., 2012, A&A, 538, A82

Roy A., Sutherland R. S., Krumholz M. R., Heger A., Dopita M. A., 2020, MNRAS, 494, 3861

Saltzman J., 1994, Journal of Computational Physics, 115, 153

Scalzo R. A., Ruiter A. J., Sim S. A., 2014, MNRAS, 445, 2535

Schmidt M., 1959, ApJ, 129, 243

Springel V., Yoshida N., White S. D. M., 2001, New A, 6, 79

Stone J. M., Norman M. L., 1992, ApJS, 80, 753

Stone J. M., Gardiner T. A., Teuben P., Hawley J. F., Simon J. B., 2008, ApJS, 178, 137

Stone J. M., Tomida K., White C. J., Felker K. G., 2020, ApJS, 249, 4

Teyssier R., 2002, A&A, 385, 337

Toro E., 1997, Riemann Solvers and Numerical Methods for Fluid Dynamics, doi:10.1007/b79761.

Ventura P., D'Antona F., 2011, MNRAS, 410, 2760

Walker A. R., 1999, AJ, 118, 432

Wang L., Kroupa P., Takahashi K., Jerabkova T., 2020, MNRAS, 491, 440

Yaghoobi A., Calura F., Rosdahl J., Haghi H., 2022, MNRAS, 510, 4330

Ziegler U., 2005, A&A, 435, 385

de Mink S. E., Pols O. R., Langer N., Izzard R. G., 2009, A&A, 507, L1

Appendix A

Phase diagrams

A phenomenon preceding star formation is the satisfying, by a gas clump, of the Jeans instability condition. This states that if an instability with a wavelength λ exceeds the Jeans length scale (λ_J), gravitational collapse will occur:

$$\lambda > \lambda_J = \left(\frac{\pi c_s^2}{G\rho}\right)^{1/2}$$

where c_s^2 is the gas sound speed, G is the gravitational constant and ρ is the gas density.

A common issue in hydrodynamic simulations that incorporate star formation is artificial fragmentation, which may occur when cold gas reaches high densities. In such cases, numerical perturbations arising from the discrete nature of self-gravitational hydrodynamics equations can grow into non-physical clumps. Truelove et al. (1997) demonstrated that artificial clumps can be avoided when the Jeans length (λ_J) is greater than or equal to 4 times the minimum cell width (Δx).

To investigate the presence of such perturbations in our models, we created density-temperature phase diagrams for the last timestep of the simulations (Figure A.1) - 55 Myr for low-density cases (M5-Infall24; M6-Infall24) and 50 Myr for the high-density case (M6-Infall23). The analysis applies the Jeans instability condition used by Calura et al. (2022), representing the analytic relation between T and ρ obtained by requiring that the Jeans length is resolved by at least 4 cells:

$$T_{Jeans} \geq \frac{\rho}{m_H}\left(\frac{4\Delta x}{16\ pc}\right)^2$$

where m_p is the mass of the proton. The figure shows that our simulations are not affected by artificial fragmentation.

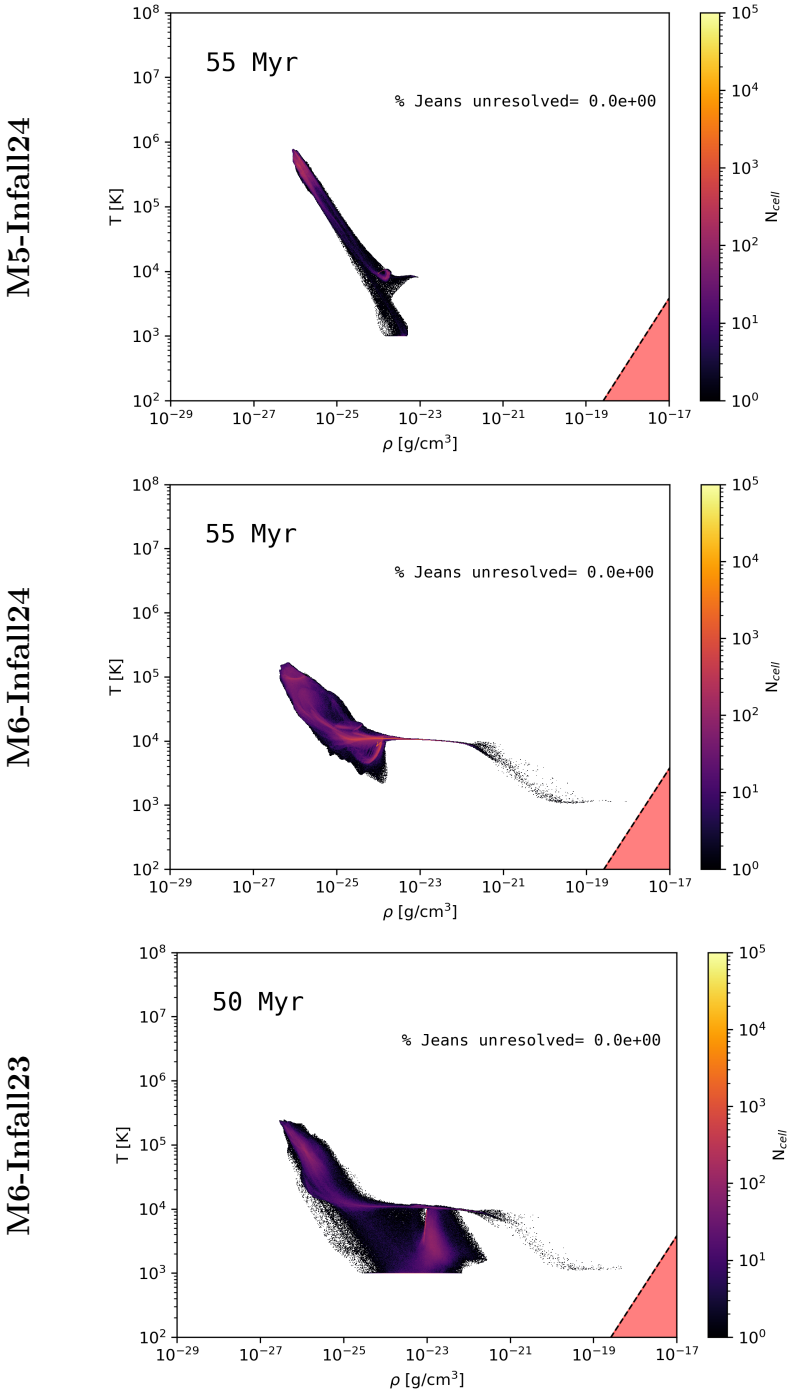

Figure A.1. Temperature–density phase diagrams in our three simulations. The oblique dashed line represents the analytical relation below which (red region) the Jeans scale is not resolved. In each panel, the fraction of cells that do not resolve the Jeans scale is shown in the top right corner. The models are indicated on the left of each set of panels. From top to bottom: M5-Infall24, M6-infall24, M6-Infall23.